

August 2016

## Measurement of Neutron Activation from a High Energy Varian Linear Accelerator

Timothy Thatcher  
*University of Nevada, Las Vegas*

Follow this and additional works at: <https://digitalscholarship.unlv.edu/thesesdissertations>



Part of the [Medicine and Health Sciences Commons](#), and the [Nuclear Commons](#)

---

### Repository Citation

Thatcher, Timothy, "Measurement of Neutron Activation from a High Energy Varian Linear Accelerator" (2016). *UNLV Theses, Dissertations, Professional Papers, and Capstones*. 2810.  
<http://dx.doi.org/10.34917/9302970>

This Thesis is protected by copyright and/or related rights. It has been brought to you by Digital Scholarship@UNLV with permission from the rights-holder(s). You are free to use this Thesis in any way that is permitted by the copyright and related rights legislation that applies to your use. For other uses you need to obtain permission from the rights-holder(s) directly, unless additional rights are indicated by a Creative Commons license in the record and/or on the work itself.

This Thesis has been accepted for inclusion in UNLV Theses, Dissertations, Professional Papers, and Capstones by an authorized administrator of Digital Scholarship@UNLV. For more information, please contact [digitalscholarship@unlv.edu](mailto:digitalscholarship@unlv.edu).

# MEASUREMENT OF NEUTRON ACTIVATION FROM A HIGH ENERGY VARIAN LINEAR ACCELERATOR

By

Timothy Richard Thatcher

Bachelor of Science – Physics  
University of California, Irvine  
2009

A thesis submitted in partial fulfillment  
of the requirements for the

Master of Science – Health Physics

Department of Health Physics and Diagnostic Sciences  
School of Allied Health Sciences  
Division of Health Sciences  
The Graduate College

University of Nevada, Las Vegas  
May 2016

Copyright by Timothy Richard Thatcher, 2016  
All Rights Reserved



## **Thesis Approval**

The Graduate College  
The University of Nevada, Las Vegas

May 10, 2016

This thesis prepared by

Timothy Richard Thatcher

entitled

Measurement of Neutron Activation from a High Energy Varian Linear Accelerator

is approved in partial fulfillment of the requirements for the degree of

Master of Science – Health Physics  
Department of Health Physics and Diagnostic Sciences

Steen Madsen, Ph.D.  
*Examination Committee Chair*

Kathryn Hausbeck Korgan, Ph.D.  
*Graduate College Interim Dean*

Ali Meigooni, Ph.D.  
*Examination Committee Member*

Ralf Sudowe, Ph.D.  
*Examination Committee Member*

Yu Kuang, Ph.D.  
*Examination Committee Member*

Tony Terrell, Ph.D.  
*Graduate College Faculty Representative*

## ABSTRACT

Linear accelerators producing photons above 10 MeV may induce photonuclear reactions in high Z components of the accelerator. These liberated neutrons can then activate the structural components of the accelerator and other materials in the beam path through neutron capture reactions. The induced activity within the accelerator may contribute to additional dose to both patients and personnel. This project seeks to determine the total activity and activity per activated isotope following irradiation from a Varian medical linear accelerator at energies above 10 MeV. A Varian 21iX accelerator was used to irradiate a 30 cm x 30 cm x 20 cm solid water phantom with 15 MV x-rays. The phantom was placed at a source-to-surface distance (SSD) of 100 cm and at the center of a 20 cm x 20 cm field. Activation induced gamma spectra were acquired over a 5 minute interval after 1 and 15 minutes from completion of the irradiation. All measurements were made using a CANBERRA Falcon 5000 Portable high purity germanium (HPGe) detector. The majority of measurements were made in scattering geometry with the detector situated at 90° to the incident beam, 30 cm from the side of the phantom and approximately 10 cm from the top. A 5 minute background count was acquired and automatically subtracted from all subsequent measurements. Photon spectra were acquired for both open and MLC fields and activities for each nuclide were estimated from detector efficiencies as determined from Monte Carlo simulations. Based on spectral signatures, the following nuclides were identified:  $^{56}\text{Mn}$ ,  $^{62}\text{Cu}$ ,  $^{64}\text{Cu}$ ,  $^{82}\text{Br}$ ,  $^{99}\text{Mo}$ ,  $^{122}\text{Sb}$ ,  $^{124}\text{Sb}$ , and  $^{187}\text{W}$ . In all cases, estimated activities from the activation products were in the microcurie range.

## **ACKNOWLEDGEMENTS**

I would like to thank all of the members of my thesis advisory committee: Dr. Steen Madsen, Dr. Ali Meigooni, Dr. Ralf Sudowe, Dr. Yu Kuang, and Dr. Tony Terrell. The knowledge and guidance you have all provided was indispensable and I thank you all.

Additionally I would like to thank Mom, Dad, Christopher, Nino, Grandma, Grandpa, and Karol. I love you all and could not have done this without you.

## TABLE OF CONTENTS

ABSTRACT.....	iii
ACKNOWLEDGEMENTS.....	iv
LIST OF FIGURES .....	vi
CHAPTER 1: INTRODUCTION.....	1
1.1 Medical Linear Accelerators .....	1
1.2 Neutron Activation .....	5
1.3 Falcon Detector .....	8
1.4 Prior Research.....	10
1.5 Scope of Work .....	17
CHAPTER 2: MATERIALS AND METHODS .....	19
2.1 Experimental Procedures .....	19
2.2 Detector Efficiency Calibration .....	20
2.3 ISOCS Efficiency Calibration Software .....	21
2.4 ISOCS Modeling Process .....	22
CHAPTER 3: RESULTS .....	27
3.1 Gamma Spectra .....	27
3.2 Detector Efficiency Calibration and Modeling .....	32
3.3 Apparent Activity .....	37
CHAPTER 4: DISCUSSION .....	43
CHAPTER 5: CONCLUSION .....	48
REFERENCES .....	50
CURRICULUM VITAE .....	54

## List of Figures

Figure 1.1: Block diagram of a medical linear accelerator .....	2
Figure 1.2: Magnetron Schematic .....	3
Figure 1.3: Cross-section of a klystron .....	4
Figure 1.4: Gamma spectra obtained at isocenter 15 minutes after beam off .....	12
Figure 1.5: Schematic view of medical linear accelerator treatment head .....	14
Figure 1.6: Isotope genealogy for radionuclides .....	16
Figure 2.1: Primary experimental setup .....	19
Figure 2.2: Alternate measurement configuration .....	22
Figure 2.3: 3D representation of solid water phantom .....	24
Figure 2.4: 3D representation of tungsten source for modeling .....	25
Figure 3.1: Comparison of initial spectra after application of 1000 MU .....	28
Figure 3.2: Gamma spectra measured after total application of 16000 MU .....	30
Figure 3.3: Gamma spectra taken with detector at beam isocenter, 90° .....	31
Figure 3.4: Gamma spectra taken with detector face directly facing beam aperture .....	32
Figure 3.5: Comparison of efficiencies between ISOCS point source modeling .....	34
Figure 3.6: ISOCS generated efficiency with and without plastic source housing .....	36
Figure 3.7: Efficiency curve generated from ISOCS modeling of experimental system .....	37
Figure 3.8: Apparent activity comparison 1000 MU with no MLC .....	39
Figure 3.9: Apparent activity comparison 1000 MU with MLC .....	40
Figure 3.10: Apparent activity comparison 16000 MU with no MLC .....	40
Figure 3.11: Apparent activity comparison 16000 MU with MLC .....	41



# Chapter 1

## Introduction

### 1.1 Medical Linear Accelerators

The practice of using radiation for medical purposes began shortly after the discovery of the x-ray by Wilhelm Roentgen in 1895 (Hendee et al., 2005). Before the invention and widespread application of the  $^{60}\text{Co}$  unit in the 1950's and 60's, most external beam radiation therapy was conducted at energies up to 300 kVp (Khan & Gibbons, 2014). As time went on, the use of the kilovoltage machine was gradually phased out and the megavoltage machine became the primary source of external beam radiotherapy. Today, the use of megavoltage beams is preferred because of its superior penetrating power, but kilovoltage beams still have application for treatment of superficial skin lesions (Hendee et al., 2005; Khan & Gibbons, 2014).

Modern linear accelerators (linacs) used for external beam radiotherapy operate on the principle of using high frequency microwaves to accelerate charged particles (i.e. electrons) to high energies where they can be used specifically to treat superficial tumors or made to interact with a high-Z metal target to produce x-rays which are ideal for the treatment of deep lesions. This is the basic operating principle of the Varian 21iX linac used in the experiments conducted in this work. Although other methods of charged particle acceleration are possible, the application of high frequency microwaves used to accelerate electrons will only be discussed here. A block diagram showing the major components of a medical linac is presented in Figure 1.1.

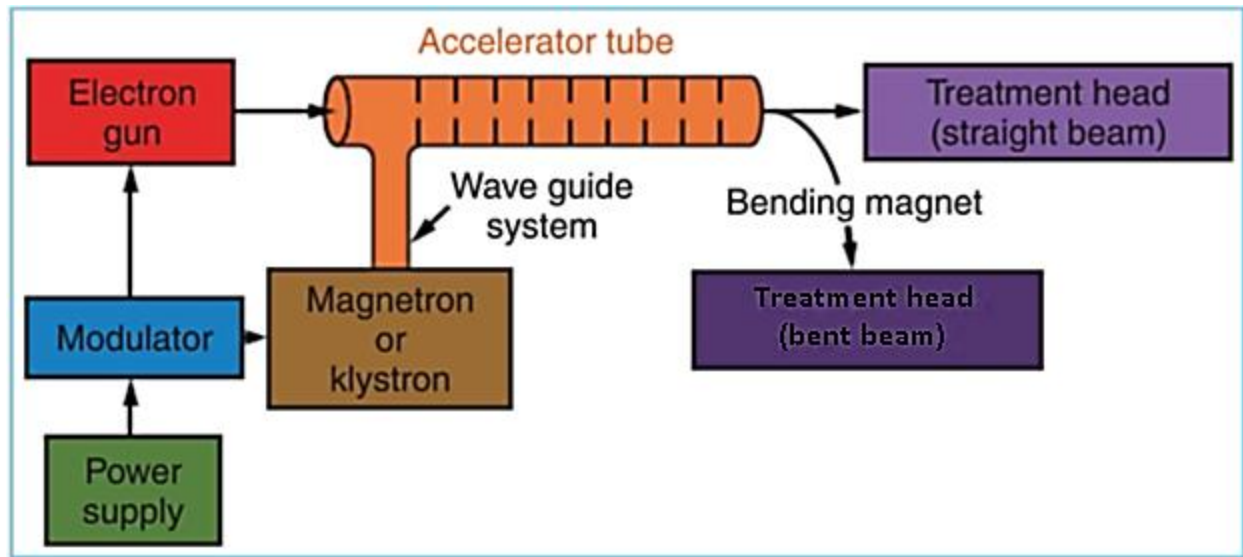


**Figure 1.1:** Block diagram of a medical linear accelerator. (Khan & Gibbons, 2014)

Linacs require a large amount of power to operate. The modulator creates direct current (DC) from the alternating current (AC) provided by the power supply. The modulator consists of both a switching tube, called a thyratron, and the pulse-forming network that will modulate this current into flat topped DC pulses of a few microseconds because linacs accelerate electrons in bursts and not as a continuous beam (Hendee et al., 2005; Khan & Gibbons, 2014). The output of these pulses is simultaneously delivered to the electron gun and the magnetron or klystron which produces the microwaves needed to accelerate the electrons.

Magnetrons are typically solid cylindrical copper anodes with a central cathode and resonant cavities bored into the wall of the cylinder. A diagram of a magnetron construction is presented in Figure 1.2. A vacuum is created between the anode and the cathode and the cathode is heated so that electrons are generated by thermionic emission. A permanent magnet supplies an axial magnetic field to the system and with each DC pulse applied the electrons are

accelerated towards the anode and move in complex spirals due to the magnetic field. Due to their spiral pathways the electrons will radiate energy in the form of microwaves which are guided to the accelerator tube by a wave guide system. Magnetrons used in linacs create microwaves of about 3000 MHz and typically provide 2-MW peak power output for lower energy linacs (6 MV or less) and up to 5-MW power for higher energies (Hendee et al., 2005; Khan & Gibbons, 2014).

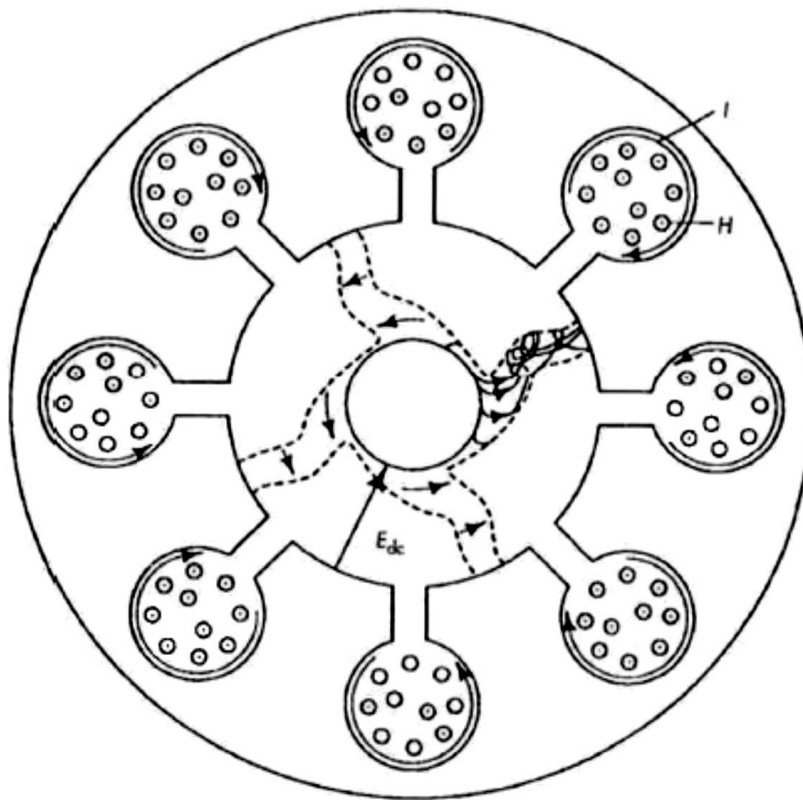


**Figure 1.2:** Magnetron schematic. (Hendee et al., 2005)

Klystrons are not generators of microwaves but instead act as microwave amplifiers and therefore need to be powered by a separate microwave oscillator (Khan & Gibbons, 2014). A

cross-sectional diagram of a klystron is provided in Figure 1.3. The application of the DC current from the pulse forming network injects electrons into the initial cavity where their velocity is modulated by the electric field of the applied low-level microwaves. This modulation causes the electrons to form bunches before they enter the field free space of the drift tube toward the “catcher” cavity. As they enter the catcher cavity they are decelerated and the kinetic energy of the electrons is transferred to higher-powered microwaves (Hendee et al., 2005; Khan & Gibbons, 2014).

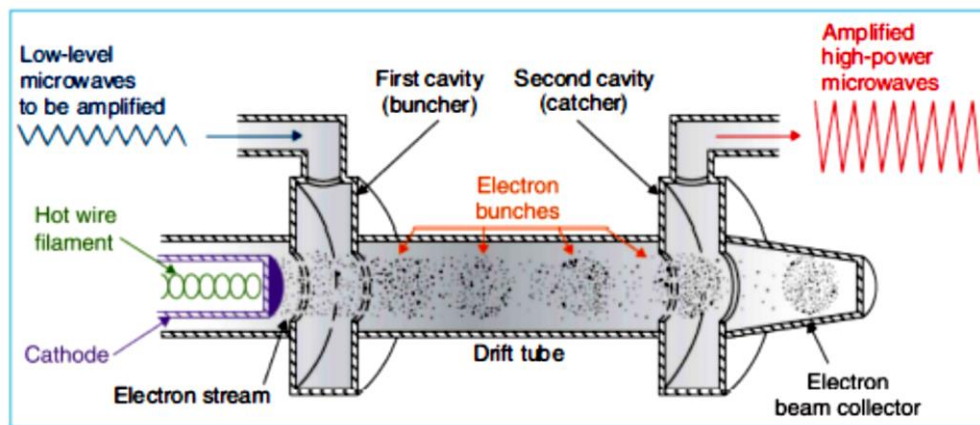


**Figure 1.3:** Cross-section of a klystron. (Khan & Gibbons, 2014)

Microwaves that are emitted from the magnetron or klystron are guided to the accelerator tube by the metal walls of the waveguide by propagating through Freon or sulfur hexafluoride (Hendee et al., 2005). The accelerator tube contains a high vacuum to prevent the electrons from interacting with gas molecules and the electron beam that exits the accelerator tube is a pencil beam of approximately 3 mm in diameter. This beam will pass through a bending magnet and then either interact with a high-Z material target such as tungsten to produce x-rays or will encounter an electron scattering foil for direct treatment using electrons. Targets used for the

production of x-rays are water cooled to prevent overheating and are at a thickness that allows for the maximum number of electron interactions with a minimum number of x-ray self-absorption.

Tests were also conducted using a Multi-leaf Collimator (MLC) with the same experimental parameters. MLC's are increasingly being used in medical linacs for intensity modulated radiation therapy (IMRT) and volumetric modulated arc therapy (VMAT) procedures because of their unique beam shaping abilities. By adding an additional collimator, photon fluence can be more properly mapped to tumor shape during the treatment planning. This has the effect of sparing surrounding tissue and providing maximum dose to the tumor volume. Prior research has shown how the addition of MLCS to the beam affects radioisotope activation (Fischer et al., 2006). The experiments reported herein similarly sought to test the influence of MLCs.

## **1.2 Neutron Activation**

The techniques and equipment used for radiation treatments of cancer have become increasingly sophisticated (Hendee et al., 2005; Khan & Gibbons, 2014; Wambersie & Gahbauer, 1996). The application of the linear accelerator for cancer treatment has allowed for radiation to be delivered at higher energies and with greater penetration and accuracy than ever before. With the introduction of techniques such as IMRT and VMAT, the energy of the radiation produced by these machines can reach energies of 20 MeV. One of the caveats of using high energies is the following; medical linacs that operate at energies above 10 MeV are capable of inducing photonuclear reactions in the high-Z components of the accelerator as well as various materials in the treatment room through photonuclear and neutron capture reactions (Ahlgren &

Olsson, 1988; Almen et al., 1991; Brusa et al., 2008; Fischer et al., 2006; Fischer et al., 2008; Kim et al., 2009; Konefal et al., 2008; Konefal et al., 2012; Ram & Steadman, 2014; Roig et al., 2004; Thomadsen et al., 2014; Yamaguchi et al., 2008). The most common photonuclear reaction is the  $(\gamma, n)$  in which a high energy photon will interact with the target nuclei resulting in the emission of a neutron. This neutron will travel a distance and will lose energy through interaction with the surrounding material until it undergoes an  $(n, \gamma)$  interaction which results in the activation of a material outside of the initial photon beam. Materials that can undergo this photoactivation include linac components, patient support systems, treatment accessories, building material, air, and the patient (Thomadsen et al., 2014). Typical radionuclides produced by the photoactivation process in a high energy radiation treatment room are summarized in Table 1.1.

Activated radioisotope	Decay mechanism	Half-life	Activation process	Photon energy (keV)	Photonuclear interaction threshold (MeV)
<sup>15</sup> O	$\beta^+$ EC	2.04 m	<sup>16</sup> O( $\gamma, n$ ) <sup>15</sup> O	511	15.66
<sup>22</sup> Na	$\beta^+$ EC	2.6 y	<sup>23</sup> Na( $\gamma, n$ ) <sup>22</sup> Na	1275	12.42
<sup>24</sup> Na	$IT, \beta^-$	15 h	<sup>23</sup> Na( $n, \gamma$ ) <sup>24</sup> Na	1369, 2754	—
<sup>27</sup> Mg	$\beta^-$	9.46 m	<sup>27</sup> Al( $n, p$ ) <sup>27</sup> Mg	844, 1015	—
<sup>28</sup> Al	$\beta^-$	2.3 m	<sup>27</sup> Al( $n, \gamma$ ) <sup>28</sup> Al	1779	—
<sup>34m</sup> Cl	$\beta^+$ EC IT	32 m	<sup>35</sup> Cl( $\gamma, n$ ) <sup>34m</sup> Cl	147, 1178, 2129	12.65
<sup>38</sup> Cl	$\beta^-$	37.24 m	<sup>37</sup> Cl( $n, \gamma$ ) <sup>38</sup> Cl	1642, 2168	—
<sup>51</sup> Cr	EC	27.7 d	<sup>50</sup> Cr( $n, \gamma$ ) <sup>51</sup> Cr	320	—
<sup>52</sup> Mn	$\beta^+$ EC	5.59	<sup>54</sup> Fe( $\gamma, np$ ) <sup>52</sup> Mn	744, 936, 1434	20.91
<sup>54</sup> Mn	$\beta^+ \beta^-$ EC	312.3 d	<sup>55</sup> Mn( $\gamma, n$ ) <sup>54</sup> Mn	835	10.23
			<sup>56</sup> Fe( $\gamma, np$ ) <sup>54</sup> Mn		20.41
<sup>56</sup> Mn	$\beta^-$	2.58 h	<sup>55</sup> Mn( $n, \gamma$ ) <sup>56</sup> Mn	847, 1811, 2113	—
<sup>53</sup> Fe	$\beta^+$ EC	8.51 m	<sup>54</sup> Fe( $\gamma, n$ ) <sup>53</sup> Fe	377	13.38
<sup>59</sup> Fe	$\beta^-$	44.5 d	<sup>59</sup> Co( $n, p$ ) <sup>59</sup> Fe	1099, 1292	—
<sup>57</sup> Co	$\beta^+$	271.8 d	<sup>59</sup> Co( $\gamma, 2n$ ) <sup>57</sup> Co	122, 136	19.3
			<sup>58</sup> Ni( $\gamma, p$ ) <sup>57</sup> Co		8.17
<sup>58</sup> Co	$\beta^+$ EC	70.78 d	<sup>59</sup> Co( $\gamma, n$ ) <sup>58</sup> Co	811, 864, 1675	10.45
			<sup>60</sup> Ni( $\gamma, np$ ) <sup>58</sup> Co		19.99
<sup>60</sup> Co	$\beta^-$	5.3 a	<sup>61</sup> Ni( $\gamma, p$ ) <sup>60</sup> Co	1173, 1333	9.86
			<sup>59</sup> Co( $n, \gamma$ ) <sup>60</sup> Co		—
<sup>57</sup> Ni	$\beta^+$ EC	35.6 h	<sup>58</sup> Ni( $\gamma, n$ ) <sup>57</sup> Ni	127, 1378, 1920	12.22
<sup>62</sup> Cu	$\beta^+$ EC	9.74 m	<sup>63</sup> Cu( $\gamma, n$ ) <sup>62</sup> Cu	876, 1173	10.85
			<sup>64</sup> Zn( $\gamma, np$ ) <sup>62</sup> Cu		18.57
<sup>64</sup> Cu	EC $\beta^- \beta^+$	12.7 h	<sup>65</sup> Cu( $\gamma, n$ ) <sup>64</sup> Cu	1346	9.91
<sup>63</sup> Zn	EC $\beta^+$	38.4 m	<sup>64</sup> Zn( $\gamma, n$ ) <sup>63</sup> Zn	670, 962, 1412	11.86
<sup>65</sup> Zn	$\beta^+$	244.3 d	<sup>66</sup> Zn( $\gamma, n$ ) <sup>65</sup> Zn	1116	11.06
<sup>82</sup> Br	$\beta^-$	35.34 h	<sup>81</sup> Br( $n, \gamma$ ) <sup>82</sup> Br	554, 619, 777	—
<sup>99</sup> Mo	$\beta^+$	66.0 h	<sup>100</sup> Mo( $\gamma, n$ ) <sup>99</sup> Mo	181, 739, 778	8.29
<sup>120</sup> Sb	$\beta^+$ EC	15.9 m	<sup>121</sup> Sb( $\gamma, n$ ) <sup>120</sup> Sb	703, 989, 1172	9.24
<sup>122</sup> Sb	$\beta^- \beta^+, EC$	2.7 d	<sup>121</sup> Sb( $n, \gamma$ ) <sup>122</sup> Sb	564, 693, 1257	—
<sup>124</sup> Sb	$\beta^-$	60.3 d	<sup>123</sup> Sb( $n, \gamma$ ) <sup>124</sup> Sb	603, 723, 1691	—
<sup>184</sup> Re	$\beta^+$	38.0 d	<sup>185</sup> Re( $\gamma, n$ ) <sup>184</sup> Re	111, 792, 903	7.67
<sup>187</sup> W	$\beta^-$	23.72 h	<sup>186</sup> W( $n, \gamma$ ) <sup>187</sup> W	134, 479, 686	—
<sup>196</sup> Au	$\beta^+$	6.2 d	<sup>197</sup> Au( $\gamma, n$ ) <sup>196</sup> Au	333, 356, 426	8.07
<sup>203</sup> Pb	$\beta^+$	51.9 h	<sup>204</sup> Pb( $\gamma, n$ ) <sup>203</sup> Pb	279, 401, 681	8.39

**Table 1.1:** Common radionuclides produced through photoactivation processes in and around medical linear accelerators. (Thomadsen et al., 2014)

There are a variety of positive and negative issues associated with the activation of materials through photonuclear reactions. For example, linac-induced photoactivation has been used for the production of various medical radioisotopes (Howard & Starovoitova, 2015; Starovoitova et

al., 2014). However, the activation of materials inside and around a linac will generally pose problems. Materials activated in a linear accelerator can cause issues to arise during decommissioning of the machine as workers may be exposed to radiation from the activation products (Brusa et al., 2008; Kim et al., 2009; Yamaguchi et al., 2008). Photoactivation of materials used in linacs can also potentially contribute to additional dose to patients and to staff (Almen et al., 1991; Fischer et al., 2008; Kim et al., 2009; Konefal et al., 2008; Yamaguchi et al., 2008). A number of studies have identified various radioisotopes produced from photoactivation, but few studies have quantified the total activity from these activated isotopes (Fischer et al., 2006; Fischer et al., 2008; Ram & Steadman, 2014).

### **1.3 Falcon Detector**

The Falcon 5000 is a high purity germanium (HPGe) detector developed by Canberra Industries which is capable of dose and count rate measurements, GPS location identification, nuclide identification from a configurable library, and gamma spectrum acquisition and analysis (Canberra Industries, 2011). It is portable and contains an ultra-low noise pulse tube cooling system capable of electrical cooling to operating temperatures of approximately -170 °C. Detector operation is conducted through wired or wireless communication with an external tablet running Windows XP with spectra analysis support with Canberra's Genie 2000 spectroscopy software.

Germanium detectors like the Falcon 5000 operate in the same fashion as other solid-state radiation detectors. The crystal lattice structure of the material creates bands of energy that



electrons may reside in. The lower band is the valence band which represents outer shell electrons bound within the crystal. The higher band is known as the conduction band and is representative of those electrons that are able to freely move within the structure. These two bands are separated by a bandgap and the size of this bandgap determines whether the material is an insulator or a semiconductor. Impurities within the crystal lattice of the detector create either an abundance of electrons (n-type) or holes (p-type). Electron-hole pairs in a semiconductor diode are analogous to ion pairs within a gas-filled detector and their motion within the detector constitutes a signal. Application of a reverse biased voltage to a system with a p-n junction allows for charge carriers created in that region to be quickly and efficiently collected (Knoll, 1999).

The Falcon 5000 HPGe was generically characterized by Canberra to be used with In Situ Object Counting System (ISOCS/LabSOCS) software packages. Detector characterization relied heavily on MCNP Monte Carlo code to simulate detector response to gamma ray sources. ISOCS characterization was conducted in three steps. The first step was to develop and validate the MCNP model to be used for the detector characterization based on the physical dimensions of the detector itself. This model was then compared with traceable sources of  $^{241}\text{Am}$  and  $^{152}\text{Eu}$  at various geometries for validation. The second step was to generate efficiency data sets at a wide variety of source locations and energies. These data sets were used in the final step, which was the creation of the detector characterization file used in the ISOCS/LabSOCS calibration software (Canberra Industries, 2011).

## 1.4 Prior Research

In 1988, Ahlgren and Olsson studied the radionuclides produced in a Varian Clinac 1800 using an 18 MV beam. Measurements were made 10 minutes after irradiation using a HPGe detector facing the target and placed at the beam isocenter. Activation products found in the accelerator head included  $^{24}\text{Na}$ ,  $^{28}\text{Al}$ ,  $^{54}\text{Mn}$ ,  $^{56}\text{Mn}$ ,  $^{57}\text{Ni}$ ,  $^{53}\text{Fe}$ ,  $^{59}\text{Fe}$ ,  $^{58}\text{Co}$ ,  $^{62}\text{Cu}$ ,  $^{64}\text{Cu}$ ,  $^{82}\text{Br}$ ,  $^{122}\text{Sb}$ , and  $^{187}\text{W}$ . Radionuclides were also found in various accelerator accessories including the steel wedge filter ( $^{28}\text{Al}$ ,  $^{53}\text{Fe}$ ,  $^{56}\text{Mn}$ ), 60° lead wedge filter ( $^{27}\text{Mg}$ ,  $^{28}\text{Al}$ ,  $^{120}\text{Sb}$ ,  $^{122}\text{Sb}$ ,  $^{124}\text{Sb}$ ), and transparent lead-block holder ( $^{15}\text{O}$ ,  $^{34}\text{Cl}^m$ ,  $^{38}\text{Cl}$ ). They also found that the induced radiation in the accelerator head could result in an absorbed dose of 2 mGy  $\text{y}^{-1}$  to a therapist's fingers.

Almen et al. (1991) tested 5 different linacs and 2 different microtrons to determine the absorbed dose to linac technicians. It was determined that the total annual absorbed dose rate to the trunk was approximately 2.0 mGy. One-third of this dose was attributed to radiation induced in the accelerator while the remaining two-thirds was due to radiation transmitted through the treatment room walls. Shortly after treatment, the dose-rate was most affected by those radionuclides with shorter half-lives ( $^{28}\text{Al}$ ,  $^{62}\text{Cu}$ ) but, at longer times, the longer half-life radionuclides ( $^{187}\text{W}$ ,  $^{57}\text{Ni}$ ) were the primary dose contributors. Furthermore, it was observed that the absorbed dose rate was approximately two times higher at the beam isocenter compared to the dose immediately adjacent to the treatment couch.

In 2004, a study of the induced activity of various components of an 18 MV Siemens KDS linac was conducted (Roig et al., 2004). Activation products were found in the target, window wave-guide, flattening filter, and wedge. These radionuclides are presented in Table 1.2.

Linac components	Radionuclide	Half-life (days)	Energy (keV)	Estimated activities and uncertainty ( $k = 2$ ) (kBq)
Target	XR Au		65–77	
	$^{196}\text{Au}$	6.2	333.0	$7100 \pm 710$
	$^{196}\text{Au}$		355.7	
	$^{196}\text{Au}$		426.1	
	$^{54}\text{Mn}$	312	834.8	$27 \pm 8.1$
Window wave-guide	$^{57}\text{Co}$	272	122.0	$16 \pm 1.9$
	$^{57}\text{Co}$		136.5	
	$^{51}\text{Cr}$	28	320	$11 \pm 1.8$
	$^{196}\text{Au}$	6.2	333	$18 \pm 2.2$
	$^{196}\text{Au}$		355.7	
	$^{196}\text{Au}$		426.1	
	$^{198}\text{Au}$	2.69	411	
	$^{58}\text{Co}$	70.86	810.7	$3 \pm 0.3$
	$^{54}\text{Mn}$	312	834.8	$3 \pm 0.4$
	$^{60}\text{Co}$	1925	1174	$11 \pm 1.1$
	$^{60}\text{Co}$		1333	$1 \pm 0.2$
Flattening filter	$^{57}\text{Co}$	272	122.0	$45 \pm 5.4$
	$^{57}\text{Co}$		136.5	
	$^{51}\text{Cr}$	28	320.0	$37 \pm 17.4$
	$^{54}\text{Mn}$	312	834.8	$40 \pm 5.2$
Wedge	Only background peaks were identified			

**Table 1.2:** Activation products found in an 18MV Siemens KDS linac for a counting time of 600s. (Roig et al., 2004)

The activities found in Table 1.2 were estimated from the set of measurements the team made seven days after the accelerator’s last clinical use. In this study, the accelerator was broken down and the component parts measured individually. Component orientation was found to not significantly affect detector signal. Not surprisingly, it was determined that the most activated component of the linear accelerator head was the target, which in this machine was made of gold and tantalum.

Fischer et al. (2006) studied the effect of open and closed collimator jaws on activation products produced and their transmission. An HPGe detector was placed on the treatment couch after delivery of 400 MU of 15MV x-rays at a dose rate of 400 MU/min. The most sensitive portion of the detector was placed near the isocenter and gamma spectra were recorded for both open jaws (field size of 15 cm x 15 cm) and closed jaws (field size below 1 mm x 1 mm). Identified radionuclides included  $^{24}\text{Na}$ ,  $^{28}\text{Al}$ ,  $^{54}\text{Mn}$ ,  $^{56}\text{Mn}$ ,  $^{57}\text{Co}$ ,  $^{58}\text{Co}$ ,  $^{60}\text{Co}$ ,  $^{57}\text{Ni}$ ,  $^{62}\text{Cu}$ ,  $^{65}\text{Zn}$ ,  $^{82}\text{Br}$ ,  $^{122}\text{Sb}$ ,  $^{124}\text{Sb}$ ,  $^{187}\text{W}$ , and  $^{196}\text{Au}$ . Discrepancies between the open and closed spectrum are shown in Figure 1.4.

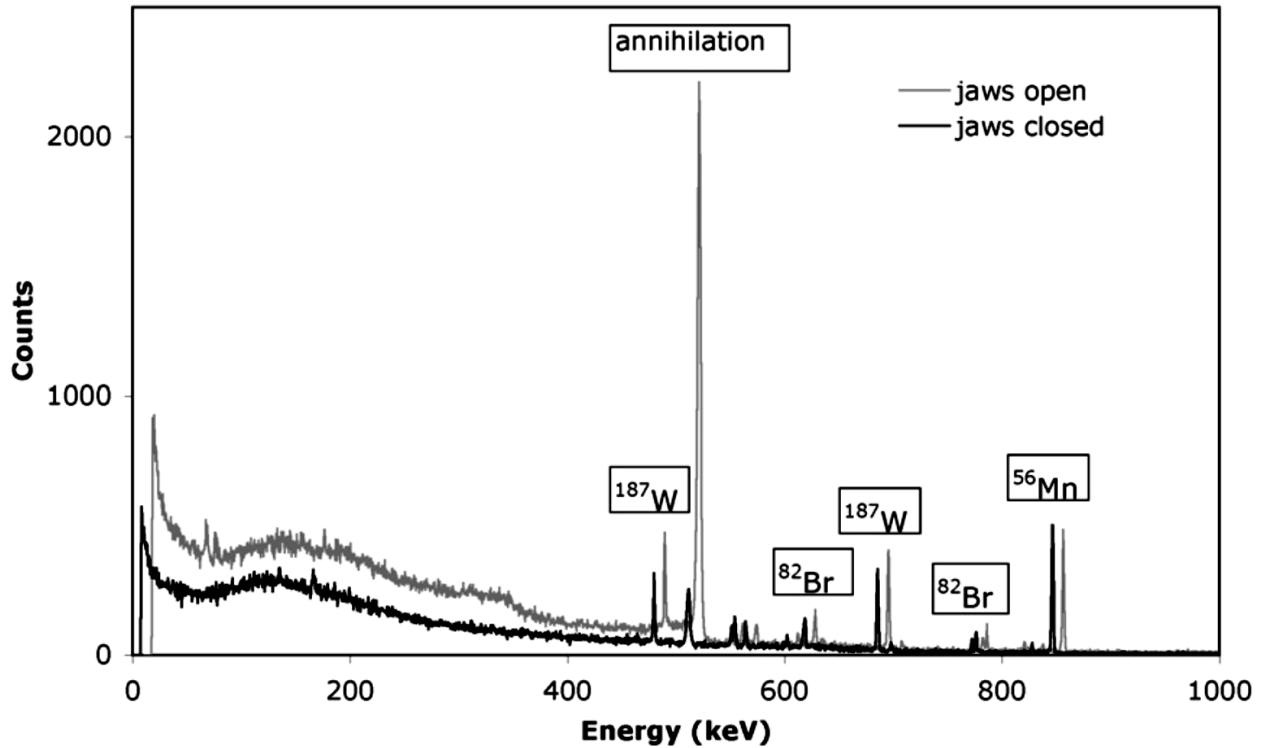


**Figure 1.4:** Gamma spectra obtained at isocenter 15 minutes after beam-off. Field size of 15 cm x 15 cm with open jaws, less than 1 mm x 1 mm with jaws closed. Open jaw spectrum shifted +10 keV for better clarification. (Fischer et al., 2006)

These results were interesting for a number of reasons. First, the count rate for the 511 keV annihilation peak was reduced significantly (~10% of initial value) with the closing of the jaws. Second, blade position was largely ineffective for reducing the spectral line amplitude of  $\beta^-$  decaying isotopes. Third, closing of the collimator had the effect of decreasing spectral line amplitude for  $\beta^+$  and EC decaying isotopes (Fischer et al., 2006). They concluded that activation products inside the linac treatment head was due primarily to photonuclear reactions and that neutron capture will largely contribute to induced activity outside the treatment head.

In 2008, Brusa et al. analyzed the long term activation produced in the treatment head of a 15 MV Mevatron Siemens 77 medical linac one year after its last clinical use. Ten different components of the treatment head were analyzed for radionuclide activity including the 270° deviation chamber, accelerating waveguide terminal, two external shields, target sledge, scattering foil support, sledge stirrup, primary photon collimator, flattening filter, and jaw. Figure 1.5 provides a schematic view of the treatment head and analyzed samples. From these measurements it was shown that one year after the medical linacs last clinical use, the bulk of the material exhibited a specific activity of less than 1 Bq g<sup>-1</sup>. Common radioisotopes found in the materials included <sup>54</sup>Mn, <sup>57</sup>Co, <sup>58</sup>Co, <sup>60</sup>Co, <sup>65</sup>Zn, <sup>181</sup>W. They concluded that most of the activated materials are metals that can be shielded and should not pose a problem (Brusa et al., 2008).

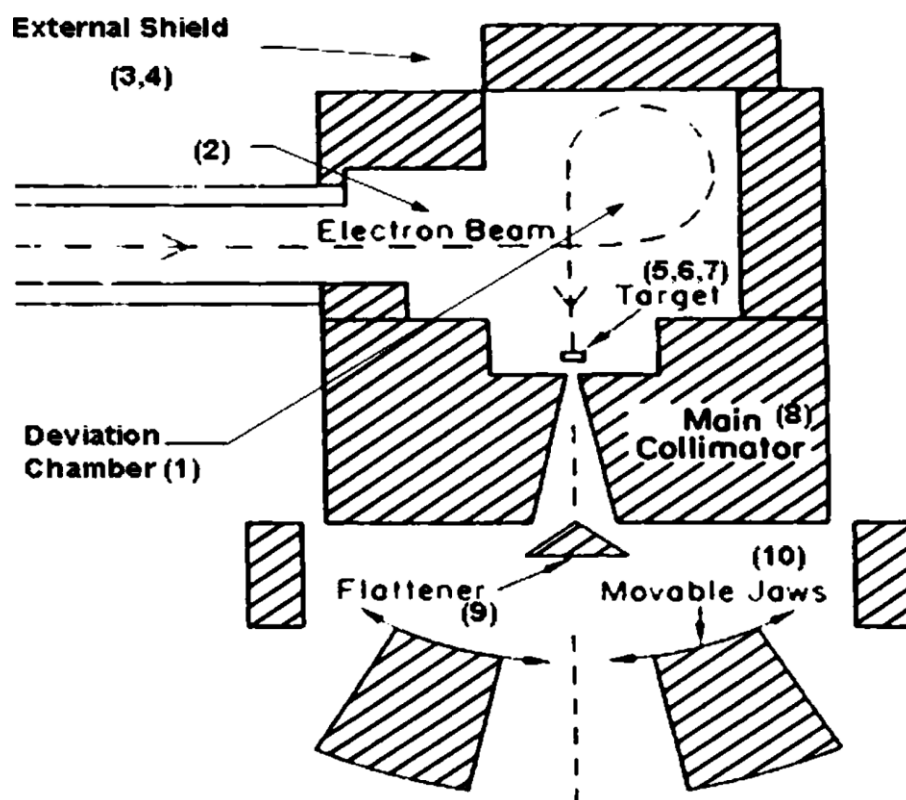


**Figure 1.5:** Schematic view of medical linear accelerator treatment head and material samples analyzed. (Brusa et al., 2008)

2008 also saw Fischer et al. (2008) compare the activation products of four different medical linacs through in situ gamma spectroscopy. Dose rates and activation products of medical linacs developed by Elekta/Phillips, General Electric, Siemens, and Varian were studied. Many of the same radioisotopes were found among the different machines and their apparent activities and dose rates calculated (Table 1.3). Of interest is the similarity in activated nuclides present within each of the different machines and the wide range of radionuclide half-lives present.

Isotope	$T_{1/2}$	Decay mode	$\Gamma$ mSv m <sup>2</sup> h <sup>-1</sup> GBq <sup>-1</sup>	A			B			C			D		
				$A_{app}$ MBq	Error %	Dose rate $\mu$ Sv h <sup>-1</sup>	$A_{app}$ MBq	Error %	Dose rate $\mu$ Sv h <sup>-1</sup>	$A_{app}$ MBq	Error %	Dose rate $\mu$ Sv h <sup>-1</sup>	$A_{app}$ MBq	Error %	Dose rate $\mu$ Sv h <sup>-1</sup>
<sup>24</sup> Na	15.0 h	—	0.429	0.052	3.9	0.022	0.060	3.7	0.026	0.008	9.5	0.0034	0.036	4.7	0.0156
<sup>28</sup> Al	2.3 m	—	0.222	1.85	6.0	0.41	4.3	4.6	0.95	2.30	5.7	0.51	9.79	19.2	2.17
<sup>51</sup> Cr	27.7 d	+	0.0042	0.124	16.5	0.0005	0.40	4.0	0.0017	n.d.			n.d.		
<sup>54</sup> Mn	312.3 d	+	0.11	0.073	2.4	0.008	0.13	2.8	0.015	0.024	4.5	0.0026	0.0058	12.3	0.0006
<sup>56</sup> Mn	2.6 h	—	0.23	0.63	3.3	0.145	1.25	3.1	0.29	0.131	4.3	0.030	0.69	3.3	0.160
<sup>57</sup> Co	271.8 d	+	0.0133	0.049	6.1	0.0006	0.144	2.7	0.0019	0.0132	7.3	0.0002	0.012	9.5	0.0002
<sup>57</sup> Ni	36.0 h	+	0.255	0.085	13.0	0.022	0.35	3.1	0.090	0.260	2.8	0.066	0.144	3.0	0.037
<sup>58</sup> Co	70.9 d	+	0.129	0.0113	9.1	0.0015	0.037	3.9	0.0048	0.005	42.0	0.0006	0.025	4.8	0.0032
<sup>59</sup> Fe	45.1 d	—	0.147	0.007	16.3	0.001	0.019	7.3	0.0028	0.005	16.0	0.0007	0.0065	23.5	0.001
<sup>60</sup> Co	5.3 y	—	0.307	0.009	13.1	0.0028	0.040	3.5	0.0122	0.0079	8.3	0.0024	0.0097	8.2	0.003
<sup>65</sup> Cu	9.7 m	+	0.151	1.50	5.0	0.226	0.54	5.5	0.082	0.59	6.0	0.090	3.21	3.3	0.48
<sup>64</sup> Cu	12.7 h	—, +	0.029	3.78	20.5	0.110	n.d.			0.76	47.7	0.022	5.4	9.4	0.160
<sup>65</sup> Zn	244.3 d	+	0.073	0.006	18.7	0.0004	0.013	9.0	0.0009	0.015	6.0	0.0011	0.0127	9.1	0.0009
<sup>82</sup> Br	35.5 h	—	0.343	0.059	3.7	0.0203	0.009	24.2	0.0031	0.091	4.2	0.031	0.105	3.4	0.0360
<sup>90</sup> Mo	66.0 h	—	0.034	0.008	13.3	0.0003	n.d.			0.008	13.3	0.0003	n.d.		
<sup>122</sup> Sb	2.7 d	—, +	0.069	0.088	5.4	0.0061	0.040	4.5	0.0028	0.0089	13.2	0.0006	0.081	4.5	0.0056
<sup>124</sup> Sb	60.2 d	—	0.26	0.0318	3.8	0.008	0.0116	6.3	0.003	0.0014	16.3	0.0004	0.024	6.3	0.0061
<sup>184</sup> Re	38.0 d	+	0.129	0.077	7.1	0.01	n.d.			n.d.			n.d.		
<sup>187</sup> W	23.7 h	—	0.073	0.72	3.9	0.053	0.24	4.9	0.018	0.134	5.7	0.0098	1.09	3.6	0.080
<sup>196</sup> Au	6.2 d	+	0.071	0.044	4.3	0.003	n.d.			0.079	5.8	0.0056	0.005	22.0	0.0004
<sup>203</sup> Pb	51.9 h	+	0.045	n.d.			0.021	11.5	0.001	n.d.			n.d.		

\* n.d. = not determined.

**Table 1.3:** Radioisotopes found in four different medical linacs including their dose rates and apparent activities. (Fischer et al., 2008)

Yamaguchi et al. (2008) found radioactive nuclides in the target assembly of a 10 MV linear accelerator, 20 MV microtron, and the screws of a cyclotron. Several radionuclides with relatively long half-lives were discovered such as <sup>51</sup>Cr, <sup>54</sup>Mn, <sup>59</sup>Fe, <sup>57</sup>Co, <sup>58</sup>Co, <sup>60</sup>Co, <sup>65</sup>Zn, <sup>108m</sup>Ag, and <sup>110m</sup>Ag (Yamaguchi et al., 2008)

Also in 2008, Konefal et al. conducted a study into the undesirable photonuclear, electronuclear, and neutron capture reactions that take place after high energy therapeutic beam emission. A Varian Clinac-2300 and a Primus Siemens medical linear accelerator were measured and the following radioisotopes were found: <sup>187</sup>W, <sup>56</sup>Mn, <sup>28</sup>Al, <sup>57</sup>Ni, <sup>38</sup>Cl, <sup>57</sup>Co, <sup>196</sup>Au, and the neutron activation of <sup>1</sup>H. Potential isotope genealogy was also determined and is presented in Figure 1.6.

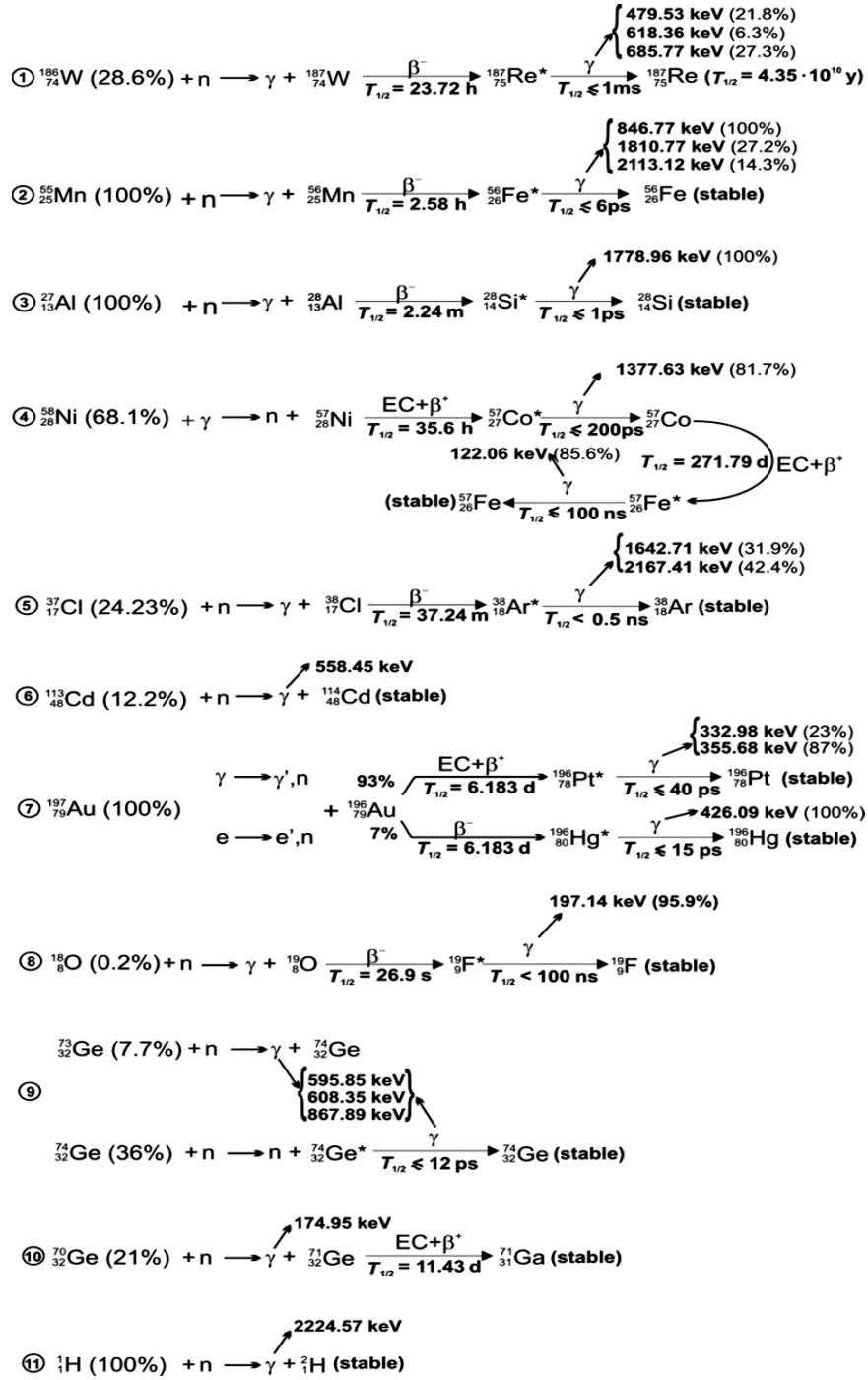


**Figure 1.6:** Isotope genealogy for radionuclides. Germanium isotopes are likely from the detector used. (Konefal et al., 2008)

Konefal et al. (2008) also determined that detector efficiency is greater when using an orientation where the detector faces the source than when its side is presented. The team also found that the



induced radioactivity in the treatment room was strongly influenced by the neutron flux and that photonuclear reactions are more likely to be induced in materials outside of heavy atomic nuclei as the x-ray beam energy increases from 15 to 20 MV.

Recently, Saeed et al. (2015) determined that direct air activation can occur in the path of a high energy photon beam.  $^{13}\text{N}$  is the main contributor to air activation from the use of a 15 MV beam and will emit a 511 keV annihilation photon after a 10 minute half-life (Saeed et al., 2015).

### **1.5 Scope of work**

This research aims to quantify the amount of activity produced by the various activated isotopes found in a Varian 21iX medical linear accelerator. Several tests were conducted in which a solid water phantom was irradiated with 15 MV x-rays for a few thousand monitor units (MU) and the activated isotopes were identified and their activities determined. To evaluate the effects of multi-leaf collimators, measurements were made with and without multi-leaf collimation. A Canberra Falcon 5000 High Purity Germanium (HPGe) detector was used to detect the gamma rays emitted from the activated isotopes. The detector position was chosen to simulate the approximate distance between a radiation therapist and patient during pre-treatment setup.

Due to the rather complex geometry associated with these experiments, ISOCS Efficiency Calibration Modeling was incorporated. This software allows for the three-dimensional modeling of radioactive sources in order to provide an efficiency curve which can be incorporated in Canberra's Genie 2000 Basic Spectroscopy and Gamma Analysis software

(Canberra Industries, 2012). The efficiency modeling was then checked against various calibration sources in order to determine the accuracy of the 3D efficiency modeling.

Based on spectral analysis, it is hypothesized that the Falcon detector is capable of identifying activation products from the Varian 21iX linac and that these isotopes are identical to those measured in other Varian linac models using different detectors. With the addition of efficiency modeling, and calibration source measurements, it is hypothesized that estimates of activities will be similar to those obtained in other studies.

## Chapter 2

### Materials and Methods

#### 2.1 Experimental Procedures

Measurements were conducted on a Varian 21iX medical linac. A 30 cm x 30 cm x 20 cm solid water phantom was placed at an SSD of 100 cm and at the center of a 20 cm x 20 cm field created by the collimator jaws of the linac. A Canberra Falcon 5000 HPGe Detector was placed 30 cm from the side of the phantom, approximately 10 cm from the top, and 90° to the incident beam along the central axis (Figure 2.1).

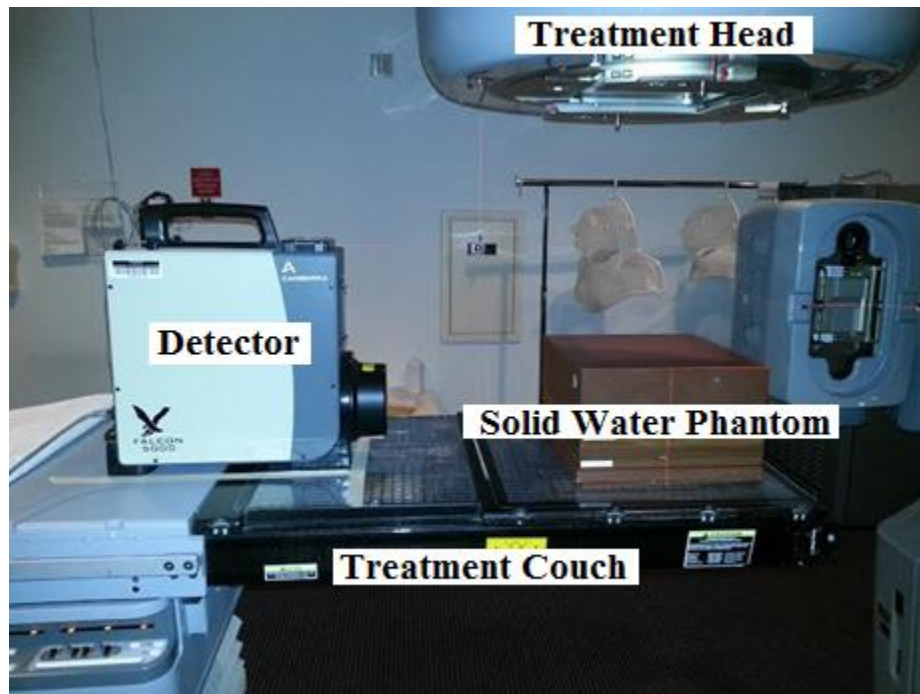


**Figure 2.1:** Primary experimental setup. Detector, solid water phantom, treatment head, and treatment couch are shown. Source-to-Surface Distance (SSD) is 100 cm.

With the detector in place and prior to beam operation, a 5 minute background count was acquired. The detector software saved this background measurement and automatically subtracted it from all subsequent measurements. The detector was then removed from the room and 15 MV x-rays were used to irradiate the phantom using both 1000 and 5000 MU. Following irradiation (1000 or 5000 MU), the detector was put into position and 5 minute spectral measurements were made within 1 and 15 minutes after the beam was shut off. These measurements were also repeated for a 20 cm x 20 cm field created using the MLC with the collimator jaws of the linac open to 25 cm x 25 cm. This was done to establish any differences in activation products between the open field and the MLC field.

In addition to the experimental setup shown in Figure 2.1, two additional 5 minute measurements were obtained: (1) with the detector placed directly underneath the central axis of the beam and (2) with the detector oriented upward directly facing the beam.

## **2.2 Detector Efficiency Calibration**

Detector efficiency calibration was conducted using three different test sources. Each test source had a known activity calibration and, taken together, the sources had gamma energies covering a wide spectrum:  $^{60}\text{Co}$  (1173 keV, 1332 keV),  $^{133}\text{Ba}$  (81 keV, 276 keV, 303 keV, 356 keV, 383 keV), and  $^{137}\text{Cs}$  (662 keV). In order to reduce scatter from the surrounding environment and optimizing the source detector geometry, the detector was positioned facing directly upward with the sources suspended above the center of the detector aperture. Measurements were conducted at distances of 30, 60, and 100 cm for each source. Acquisition time for each measurement was 2 hours. This ensured that the peak energies from each source

were prominently measured. The efficiency at each energy was calculated and used to compare the results determined from the ISOCS modeling.

### **2.3 ISOCS Efficiency Calibration Software**

ISCOS Efficiency Calibration software allows for the determination of efficiency calibration through 3D modeling in order to assess contamination levels for a variety of substances including soil, bags, drums, boxes, walls, pipes, and various metals such as lead and tungsten. Shape templates are provided by the software, and using these various templates a 3D representation of the object from which gamma spectral data was acquired can be created. With this data the ISOCS software can generate the required efficiency calibration file to be used to analyze the acquired spectra.

The issue of efficiency calibration was evident from the way that our experiment was set up. As previously discussed, the experimental geometry was chosen to mimic the geometry between the radiation therapist and patient. This involved placing the detector 90° from the central beam axis and 30 cm from a solid water phantom as illustrated in Figure 2.1. This setup was also chosen because it has been shown to provide maximum neutron flux (Howell et al., 2009). Unfortunately, this geometry made efficiency calibration particularly difficult. Other research into activation products placed the detector at an orientation where it was directly under the isocenter of the beam similar to Figure 2.2 (Fischer et al., 2006; Fischer et al., 2008; Ram & Steadman, 2014). Using this geometry, the efficiency can be calculated from a variety of test sources placed at approximately 1 m from the detector (Ram & Steadman, 2014; Roig et al.,

2004). The geometry used for the present experiment was more complex and necessitated the ISOCS software to determine the detection efficiency.

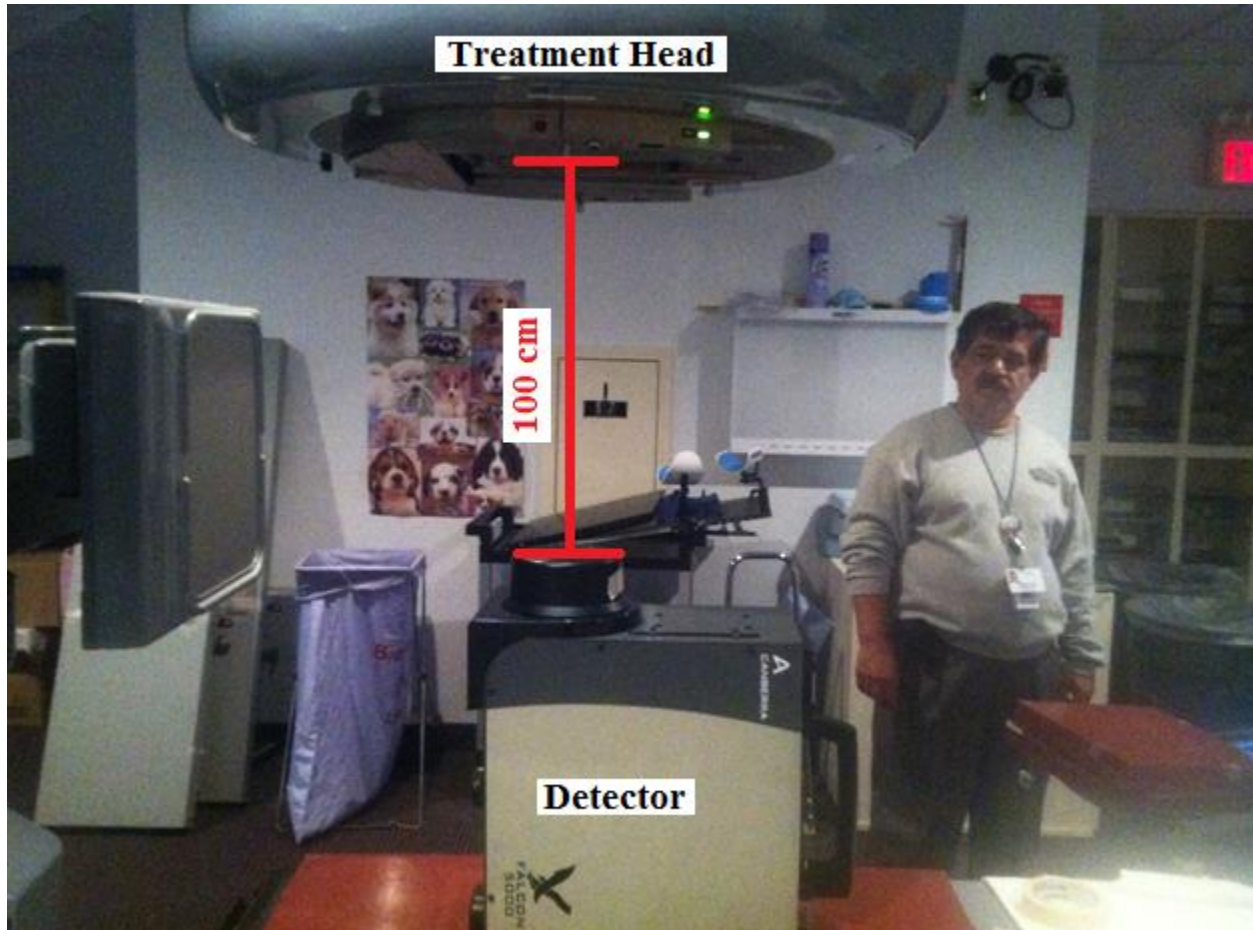


**Figure 2.2:** Alternate measurement configuration. Here the detector is directly facing the treatment head at an SSD of 100 cm.

## 2.4 ISOCS Modeling Process

Specific details about the materials used in the construction of the Varian 21IX are proprietary information of Varian Medical Systems and therefore certain assumptions had to be made regarding the materials used to construct the linac and hence the input parameters for the 3D modeling software. An attempt was also made to simplify the experimental geometry.

Although the x-ray beam is pointed in a single direction toward the patient, there exists a considerable amount of scatter which allows for radiation to propagate throughout the room. Similarly, activated radioisotopes can exist in the accessories present in the treatment room and are not exclusive to components of the linac (Fischer et al., 2006; Thomadsen et al., 2014). This uncertainty in the precise location of the emitted radiation detected necessitated a simplification in the geometry used in the 3D modeling process. A two object system was assumed: a simple sphere of tungsten representing isotropic distribution of radiation from the head of the linac, and a simple box of water representative of the solid water phantom. Prior research has found that the target and linac head are the most activated objects in the linear accelerator system and tungsten was used because that is the material generally used as the target (Brusa et al., 2008; Kim et al., 2009; Roig et al., 2004; Yamaguchi et al., 2008).

Upon running the ISOCS software one of the first prompts that appears is the choice of detector type. The Falcon 5000 HPGe and Falcon collimator cap were chosen as they have both been characterized previously by the software. From the list of available templates, Simple Box and Simple Sphere were chosen in order to model the solid water phantom and linac head, respectively. A 30 cm x 30 cm x 20 cm water box with a source concentration value of 1.0 was created and placed 30 cm from the detector (Figure 2.3).

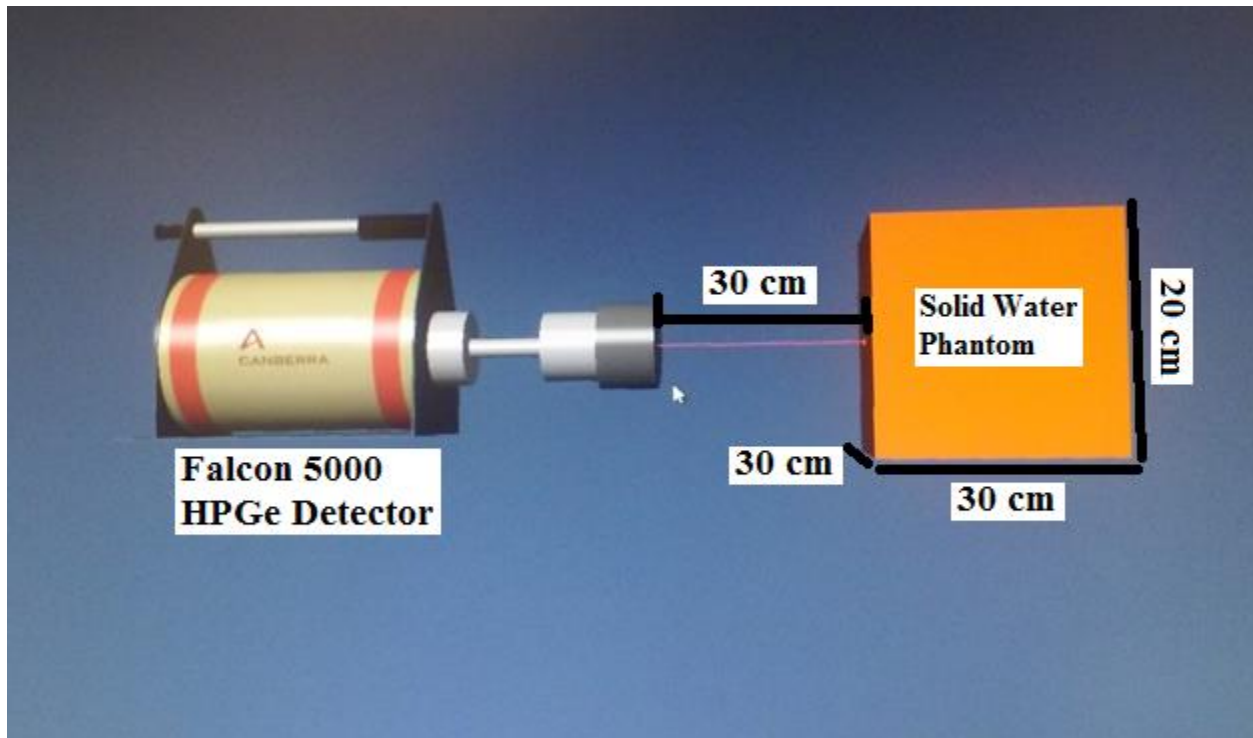


**Figure 2.3:** 3D representation of the solid water phantom of dimensions 30 cm x 30 cm x 20 cm.

A tungsten point source was modeled using the simple sphere schematic from the ISOCS software package. Although a point source is not truly representative of the actual shape and size of the target, it does provide for an approximation of the isotropic distribution of radiation emanating from the target. Using a point source also had the benefit of increasing the efficiency of the system by limiting the amount of self-attenuation present. Figure 2.4 displays an exaggerated representation of the tungsten point source in order to clarify detail and positioning in relation to the detector.



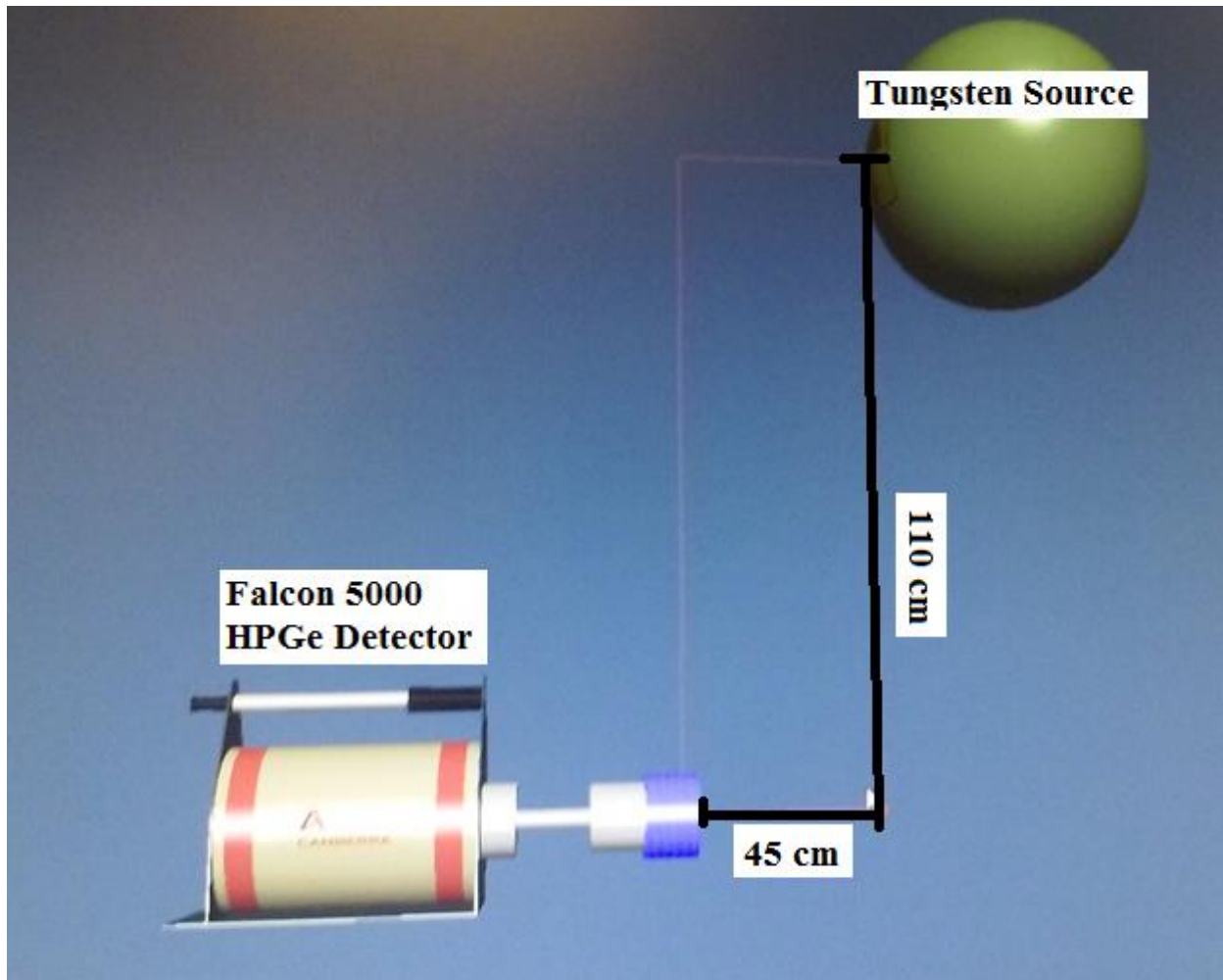


**Figure 2.4:** 3D representation of the tungsten source used for modeling. The present sphere was enlarged to display detail and location of the tungsten source. Actual modeling was conducted using a tungsten point source in order to limit the effect of self-attenuation.

Point sources of both cobalt and cesium were also simulated in order to verify the efficiency curves generated from the ISOCS modeling. These point sources were 0.1 mm diameter spheres with no wall thickness and placed 1 m from the front of the virtual detector. The source itself contained a 0.01 mm source shell thickness and a 1:1 relative source concentration ratio between the shell and the volume. To better simulate a check source used for efficiency calibration, plastic housing was also modeled and the point sources placed within

them. A simple cylinder of low density polyethylene 2.54 cm (1 inch) in diameter and 0.5 cm thick was created to act as housing for both the cesium and cobalt point sources.

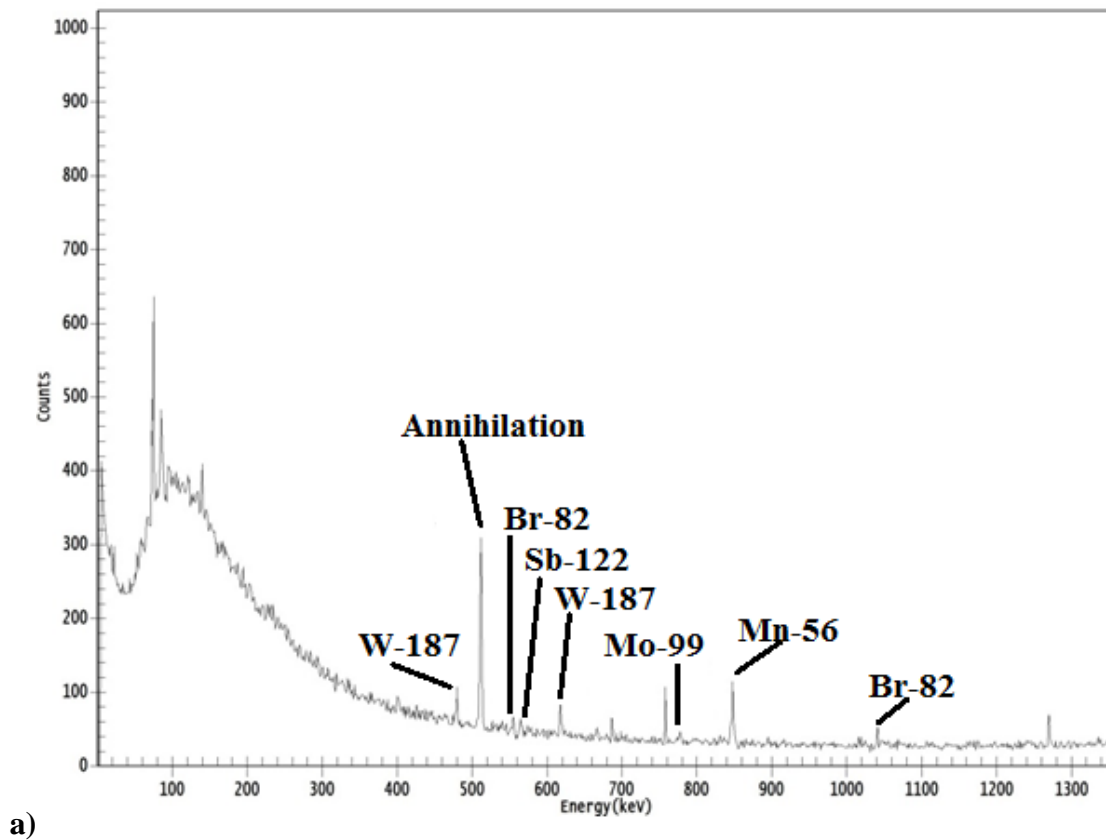
The software does not allow modeling of more than one object at a time, but it does allow for calibration of multiple sources using the Weighted Average mode once an efficiency (ECC) file is created for each object. A weighting factor proportional to the activity of each object is chosen and is generally determined by the volume of the element (Canberra Industries, 2012). This multi-efficiency process was conducted on both the sphere/box system and the point source/plastic housing system. Arbitrarily chosen weighting factors of 2:1 was used for the sphere/box system and 1:1 for the point source/plastic housing system.

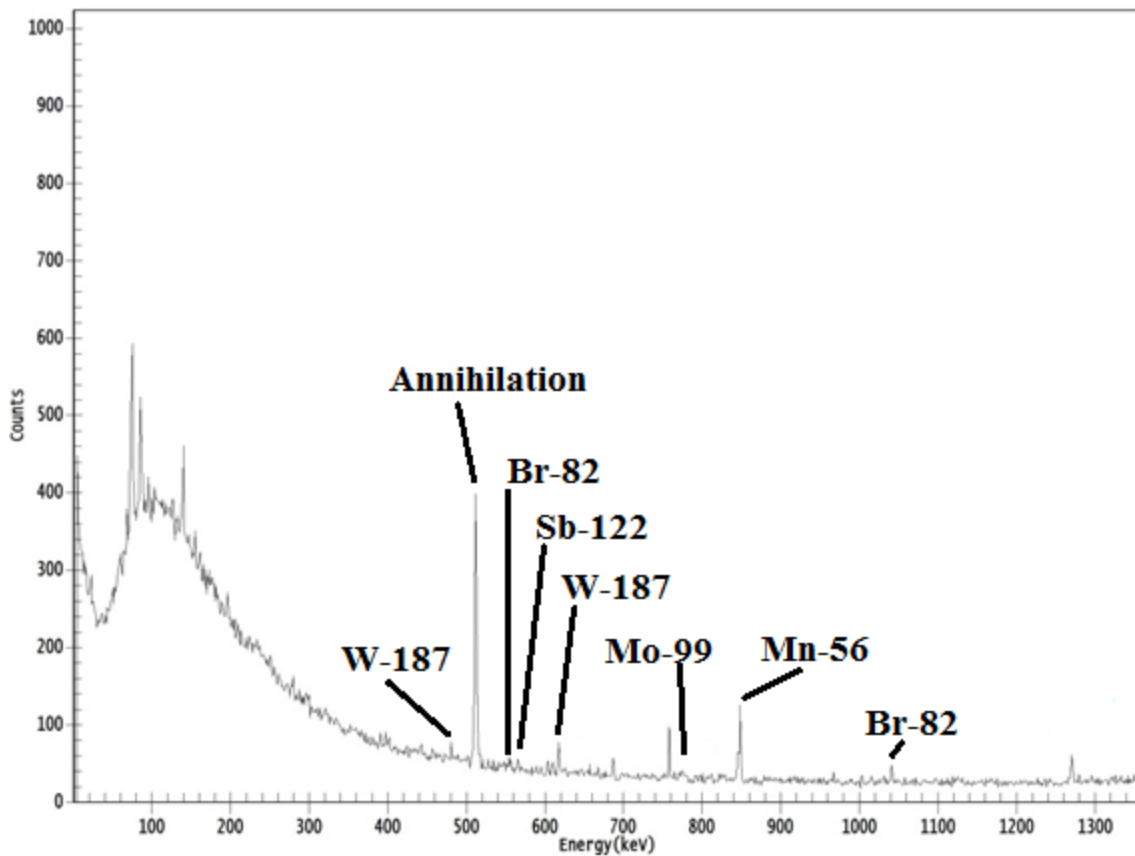
## Chapter 3

### Results

#### 3.1 Gamma Spectra

Eighteen total measurements were conducted and the gamma spectra analyzed. Eight measurements were conducted on the first day and ten measurements conducted on the second day. The first eight measurements from the second day were performed to the same specifications as the eight measurements from the first day but with the addition of MLC. Two more measurements were performed on the second day with the detector in different orientations. A comparison between the measurements from the two days is provided in Figure 3.1.

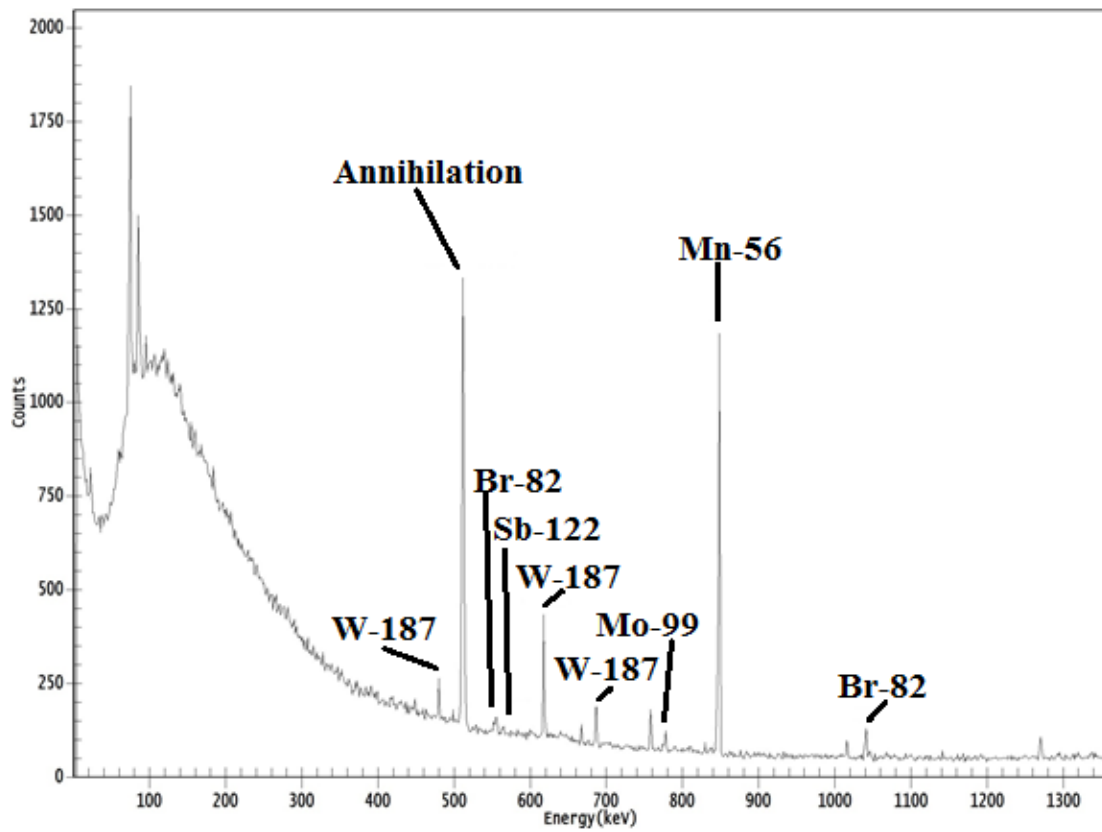




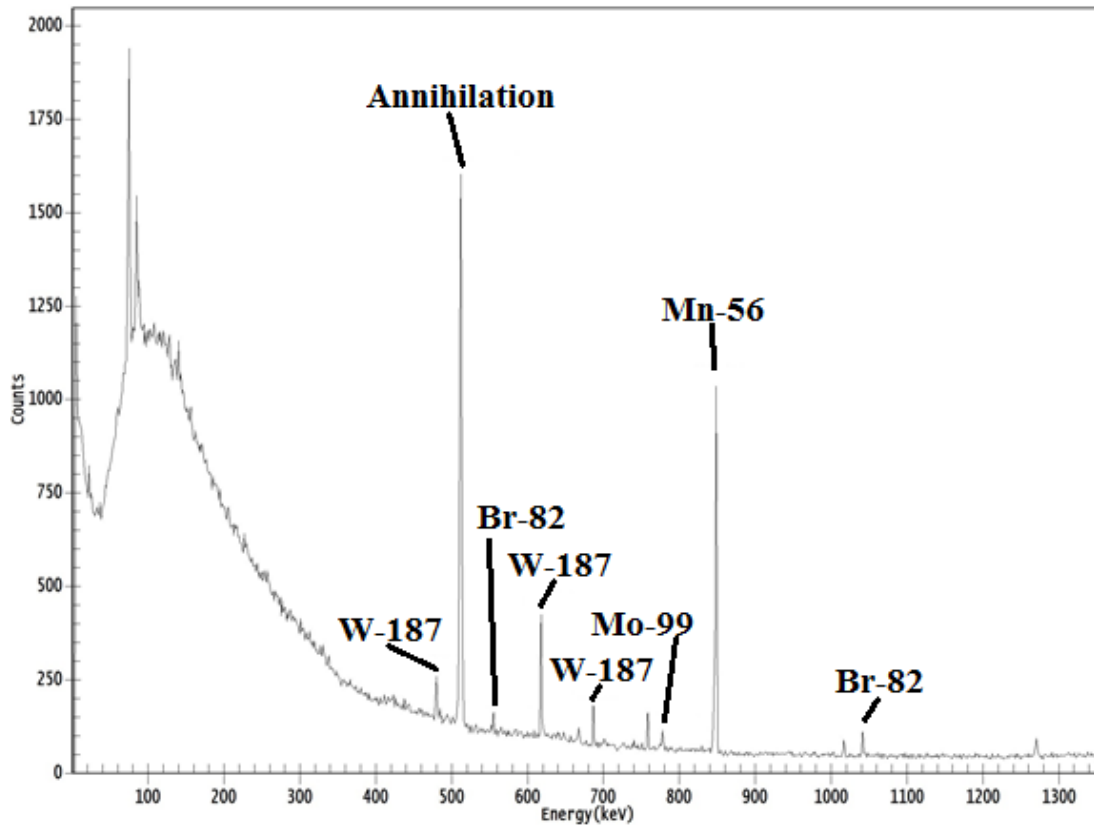
b)

**Figure 3.1:** Comparison of initial spectra after application of 1000 MU. a) Spectra taken without MLC. b) Spectra taken with MLC.

Figure 3.1 shows several similarities between the two spectra after an initial application of 1000 MU. A prominent annihilation peak and several isotopes ( $^{56}\text{Mn}$ ,  $^{82}\text{Br}$ ,  $^{99}\text{Mo}$ ,  $^{122}\text{Sb}$ , and  $^{187}\text{W}$ ) were found in both spectra with and without the application of MLCs. After an initial application of 1000 MU of radiation, there appears to be little difference between the two spectra presented. An additional 15,000 MU (Figure 3.2) resulted in several peaks becoming more defined, but the overall shape and isotopes found did not change compared to the 1000 MU data.



a)



b)

**Figure 3.2:** Gamma spectra measured after total application of 16000 MU. a) Spectra taken without MLC. b) Spectra taken with MLC.

Two measurements were taken with the detector in an alternate position in order to compare how the difference in orientation affected the spectra. In Figure 3.3, the most sensitive area of the detector was placed at the beam isocenter with an SSD of 100 cm and oriented at 90°. These measurements were taken approximately 30 minutes after the last beam operation, but it is apparent that placing the detector directly under the beam aperture allows for fairly well defined peaks of familiar isotopes. The last measurement was taken with the detector directly facing the beam aperture and is presented in Figure 3.4. Changing the detector orientation resulted in the detection of two additional isotopes:  $^{64}\text{Cu}$  (1346 keV) and  $^{124}\text{Sb}$  (1046 keV).

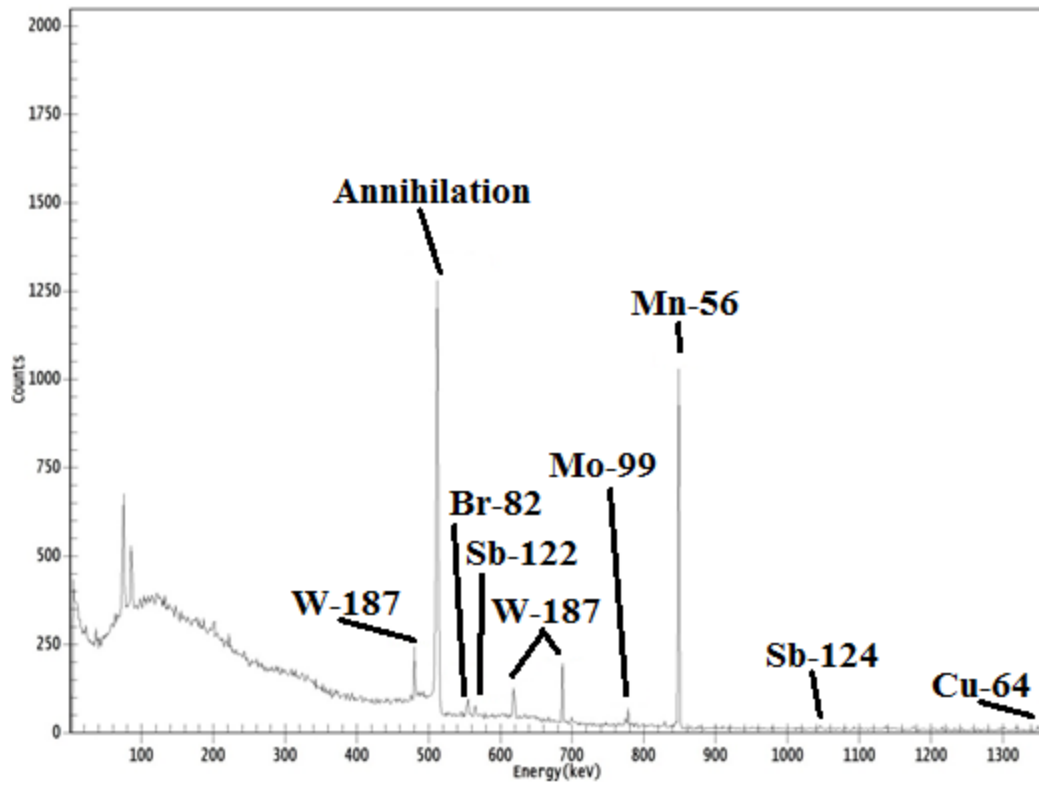


**Figure 3.3:** Gamma spectra taken with detector at beam isocenter, 90 degrees, SSD of 100 cm, and approximately 30 minutes after beam was shut off.

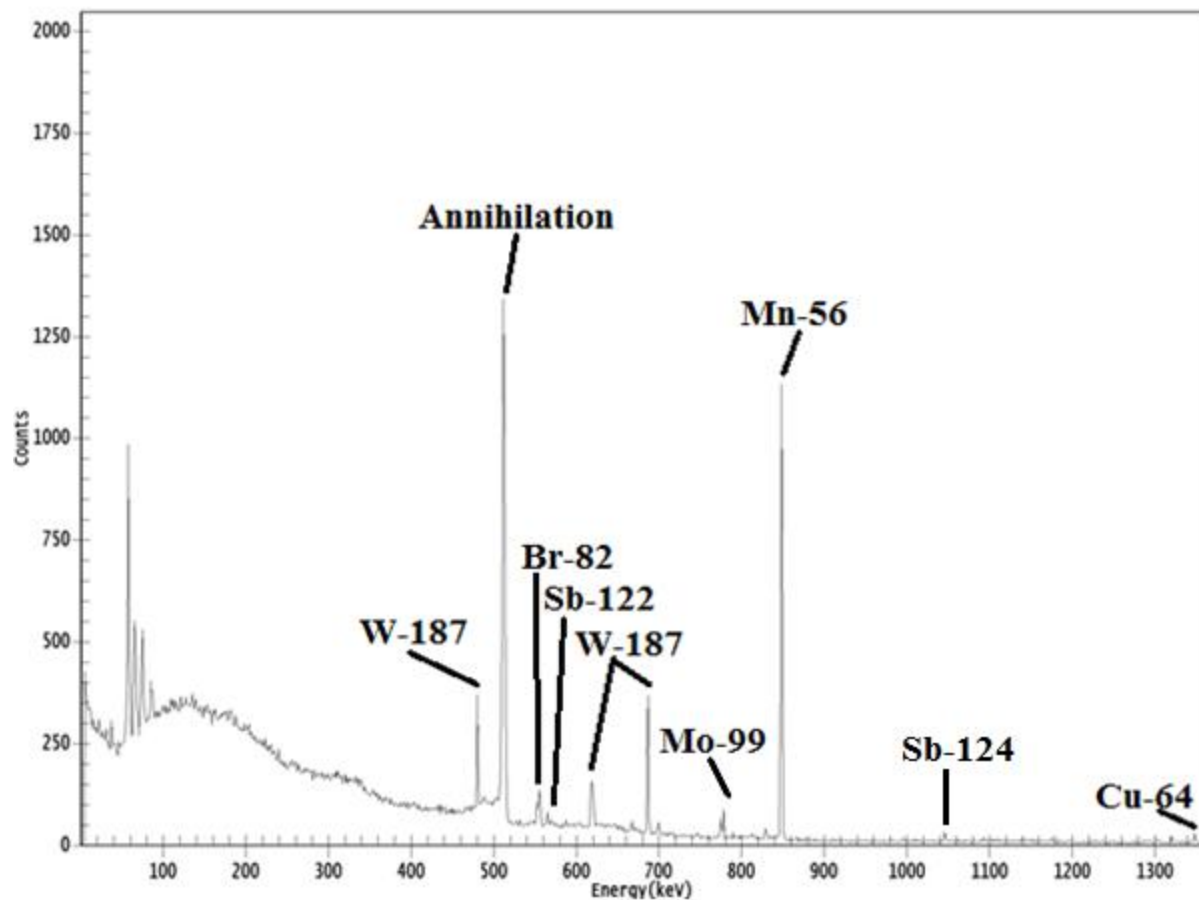


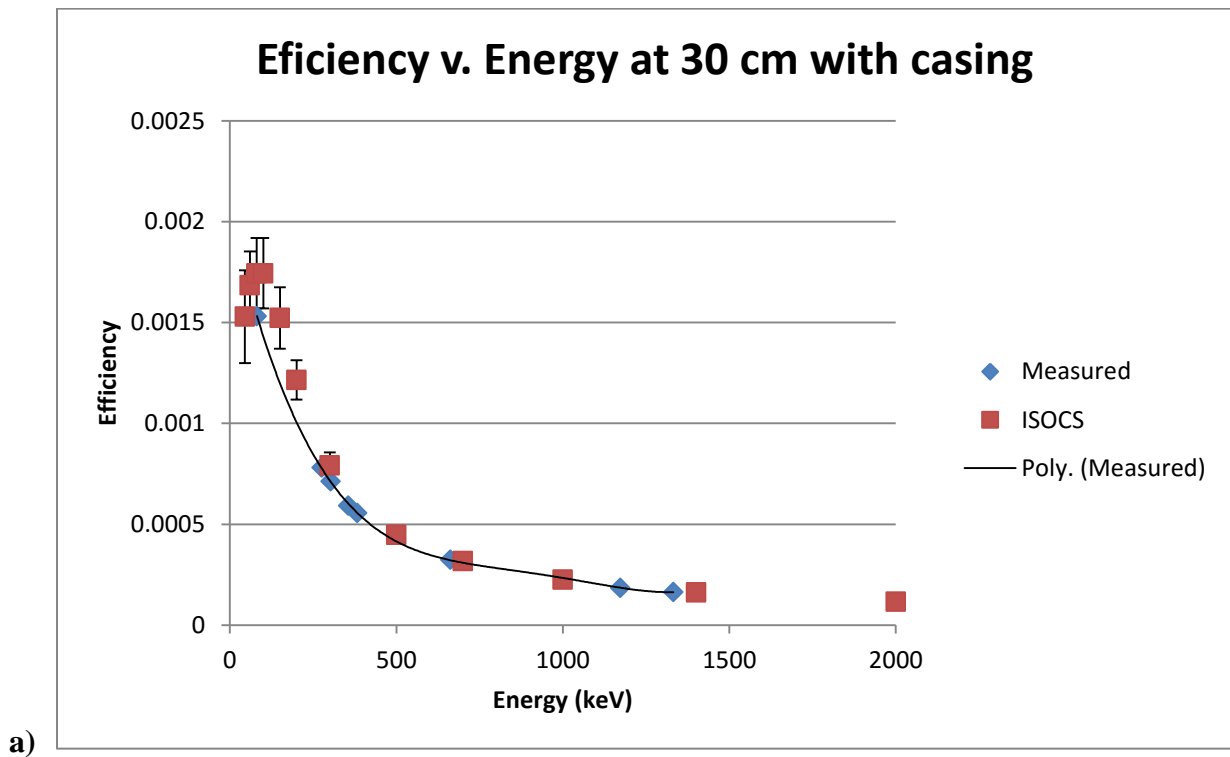
**Figure 3.4:** Gamma spectra taken with detector face directly facing beam aperture (0 deg.) approximately 40 minutes after beam off.

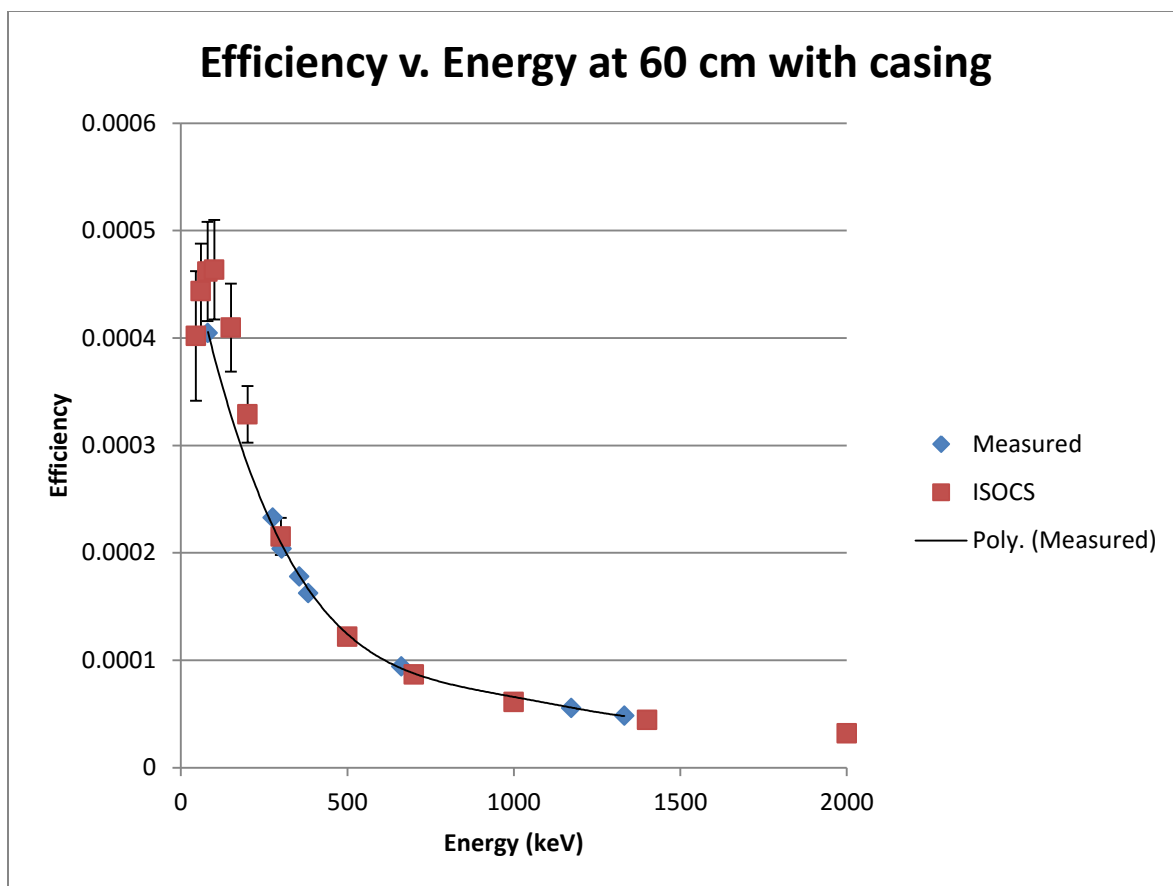
### 3.2 Detector Efficiency Calibration and Modeling

ISOCS was used to create a 3-D model of our system in order to determine the detection efficiency of the applied geometry. Prior to modeling this complex geometry, the efficacy of the ISOCS software was tested by modeling a point source and comparing it to an efficiency curve developed with multiple sources. A point source of cesium and cobalt was modeled as was the

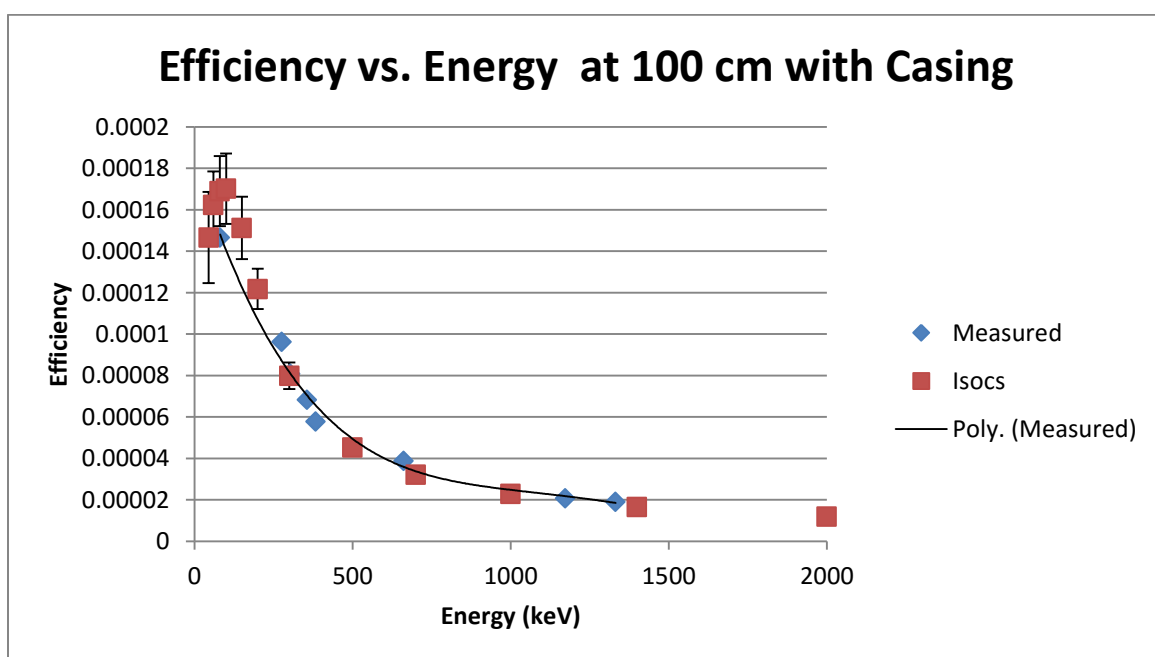


small polyethylene housing that contains these sources. The efficiency for the two modeled point sources was calculated using a 1:1:1 weighted average between the cesium, cobalt, and polyethylene housing. The efficiency curve modeled from ISOCS was compared to the data from the point source measurements using various check sources. The results from the efficiency comparison at 30, 60, and 100 cm are presented in Figure 3.5.





b)



c)

**Figure 3.5:** Comparison of efficiencies between ISOCS point source modeling and measured values of various check sources at **a)** 30 cm, **b)** 60 cm, and **c)** 100cm

The measured data was fit to a fifth order polynomial in order to compare it the ISOCS generated results and is presented in Figure 3.5 as “Poly (Measured)”. As shown in Figures a – c, there is good agreement between the ISOCS modeled results and the calibration sources at each measured distance. The comparison is more tenuous at lower energies, which could be due to a lack of data points within that range. One of the caveats to using the ISCOS software is that modeled parameters need to contain a source concentration in order for its efficiency to be determined. This includes modeled objects such as the polyethylene housing for the check sources used in the previous comparison. In order to model the entire system, a miniscule amount of source concentration was added to the polyethylene so that the efficiency could be determined. This cesium/cobalt/polyethylene system was then compared to just a cesium/cobalt system to determine the effect of the polyethylene source concentration on the total efficiency. It was shown that addition of the polyethylene source housing had no effect on the total efficiency determined by ISOCS and its subsequent fit to our measured data. This comparison is presented in Figure 3.6.

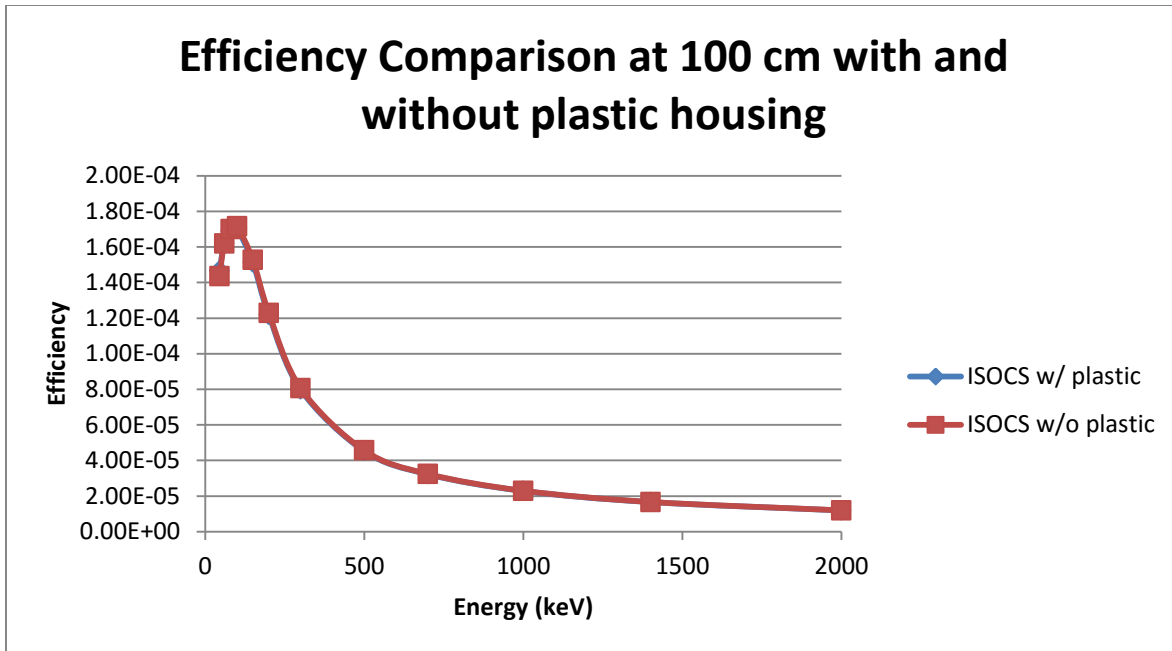


**Figure 3.6:** Comparison of the ISOCS generated efficiency with and without the addition of the plastic source housing show nearly identical results. The plastic source housing has a miniscule source concentration that evidently had little effect on the total efficiency generated.

These results help to validate the ISOCS software modeling and show that the software is capable of modeling a simple system accurately. This is a necessary first step and provides a high degree of confidence that the software is capable of modeling more complex geometries such as those used in the present experiments. As previously discussed, the efficiency curve used for the experimental geometry involved modeling a tungsten point source and a solid water phantom. (Figure 3.7).

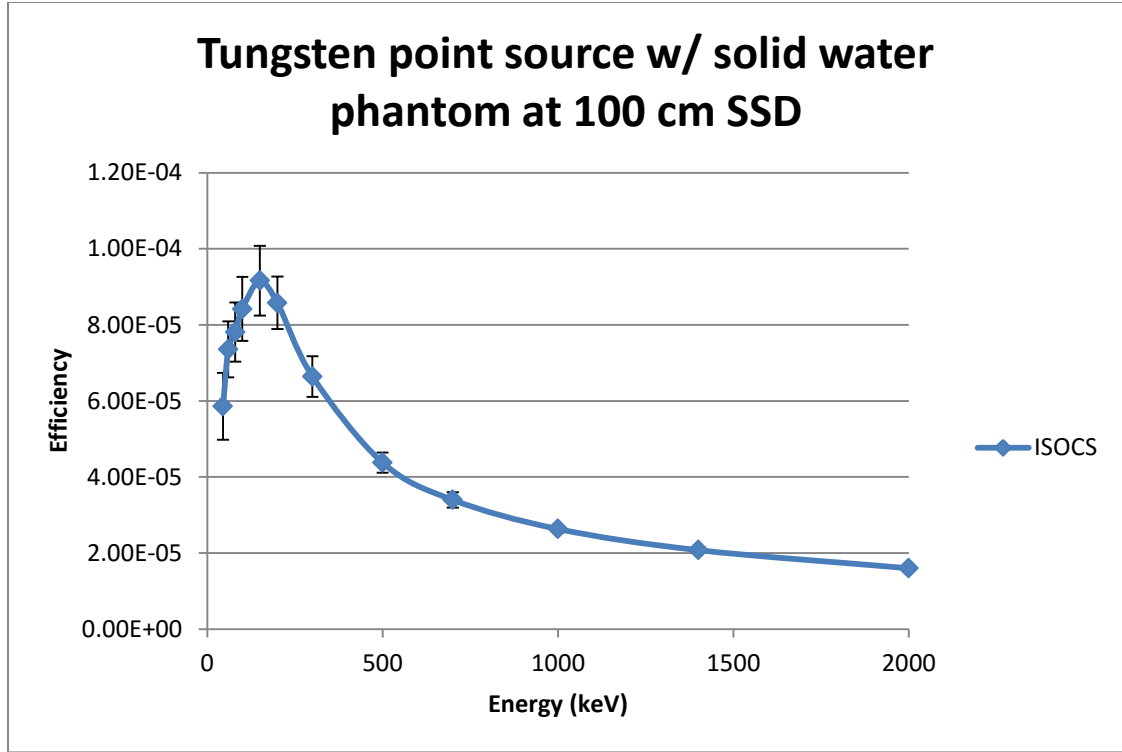


**Figure 3.7:** Efficiency curve generated from ISOCS modeling of the experimental system. These efficiencies were used to determine the apparent activities of the measured isotopes.

### 3.3 Apparent Activities

After the modeled efficiency determination, isotope apparent activities were determined by the following equation:

$$A = e^{(\lambda \Delta t)} \frac{C}{t_{live} * f * \epsilon} \quad (\text{Eq.1})$$

Where A = apparent activity in Bq,  $\lambda$  = isotope decay constant,  $\Delta t$  = time interval between beam off to spectra acquisition, C = net counts under a peak,  $t_{live}$  = live measurement time, f = branching ratio for the observed energy, and  $\epsilon$  = photopeak efficiency of the detector at the observed energy. The apparent activity equation was used by Fischer et al., (2008) in their

comparison of several different medical linacs by assuming that “all nuclei are concentrated at 1 m distance from the detector” and that “all induced activity is concentrated in the accelerator target” and gives the value of the induced activity at the time of beam termination. Although this may not necessarily be true in most cases, assuming a centralized location for the activity generated allows for quick comparison between different machines. This assumption was made in this work and the work of Ram and Steadman (2014). The observed isotopes and activities presented by Fischer et al. (2008) and Ram and Steadman (2014) are reproduced in Tables 1.3 and 3.1, respectively. Although the gamma spectra observed varied between each machine used, several isotopes were found in all studies including  $^{56}\text{Mn}$  (848 keV),  $^{82}\text{Br}$  (555, 1041 keV),  $^{122}\text{Sb}$  (564 keV), and  $^{187}\text{W}$  (480, 617, 686 keV).  $^{62}\text{Cu}$  (511 keV) was absent from the Ram and Steadman (2014) data but was present in this project’s data and the Fischer et al. (2008) data. In spite of the differences in equipment and methodology used in the different studies, these isotopes were consistently found and served as a good point of comparison.

Isotope	$T_{1/2}$	Exemption Quantity (MBq)	Activity $t = 0$ h (MBq)	Peak Energy (keV)	Intensity	Exemption Quantities $t = 0$ h	Exemption Quantities $t = 36$ h
$^{24}\text{Na}$	15.0 h	0.1	0.444	1368.63	1.0	2.813	0.533
$^{28}\text{Al}$	2.3 m	0.01	474.599	1778.97	1.0	45793.83	-
$^{56}\text{Mn}$	2.6 h	0.1	3.14	846.77	0.989	19.2	0.001
$^{57}\text{Ni}$	36.0 h	1.0	0.168	1377.63	0.817	0.120	0.06
$^{64}\text{Cu}$	12.7 h	1.0	0.175	1345.84	0.473	0.171	0.024
$^{66}\text{Cu}$	5.1 m	0.01	8.155	1039.23	0.09	815.5	-
$^{82}\text{Br}$	35.5 h	1.0	0.020	698.37	0.2849	0.028	0.014
$^{122}\text{Sb}$	2.7 d	100	0.18	564.12	0.71	0.00074	0.001
$^{124}\text{Sb}$	60.2 d	1.0	0.0016	1690.98	0.4779	0.009	0.009
$^{187}\text{W}$	23.7 h	1.0	0.657	685.73	0.332	0.944	0.329
$^{228}\text{Ac}$	6.15 h	1.0	0.113	911.20	0.258	0.113	0.002
$\Sigma$ Exemption Quantities:						46632.74	0.974

**Table 3.1:** Gamma spectroscopy results from a Varian TrueBeam medical linear accelerator. (Ram & Steadman, 2014)

Apparent activities were converted from becquerel to microcurie for comparison. Data for this project was presented in three ways: no normalization to applied MU, normalization to last applied MU, and normalization to total applied MU. Figure 3.8 and 3.9 display the comparison of apparent activities between the datasets after application of 1000 MU without and with MLC present, respectively. Figure 3.10 shows the dataset comparison without MLC after total application of the full 16000 MU while Figure 3.11 shows the data for the same parameters but with the MLC applied. Table 3.2 lists a summary of the apparent activities after total application of 16000 MU.

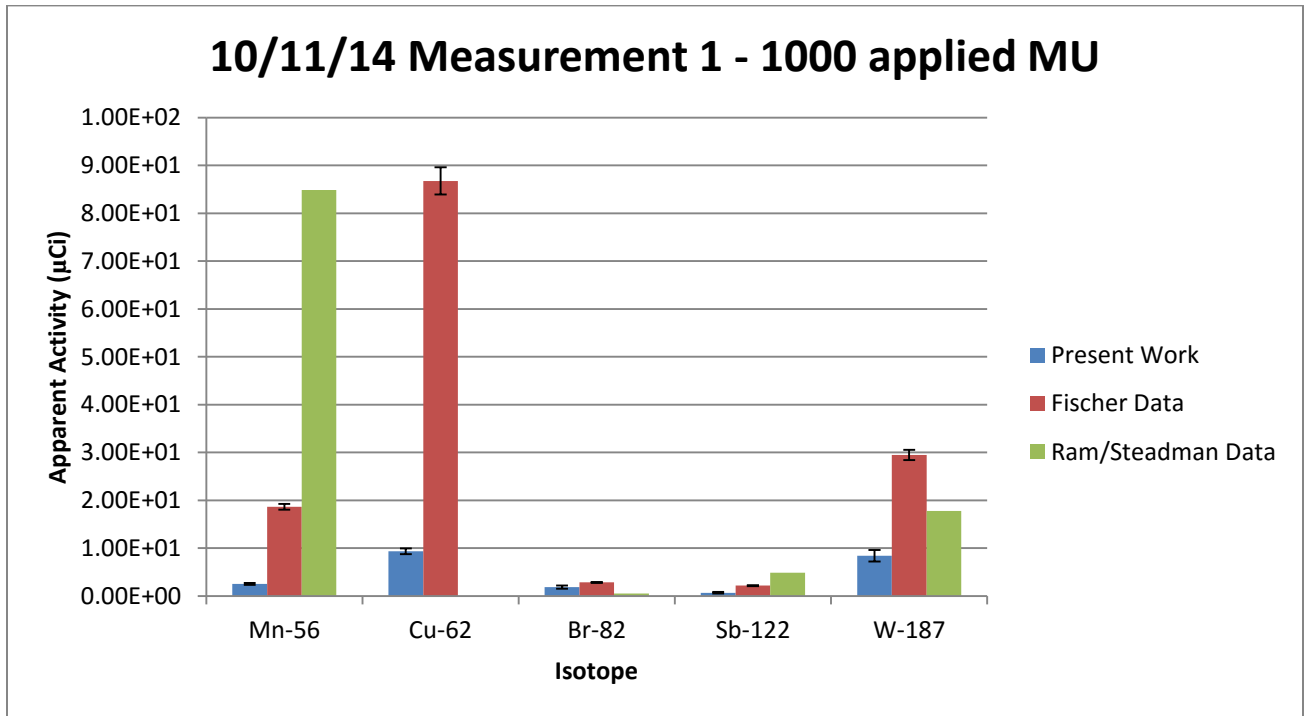


**Figure 3.8:** Apparent activity comparison between different datasets after total application of 1000 MU with no MLC present.

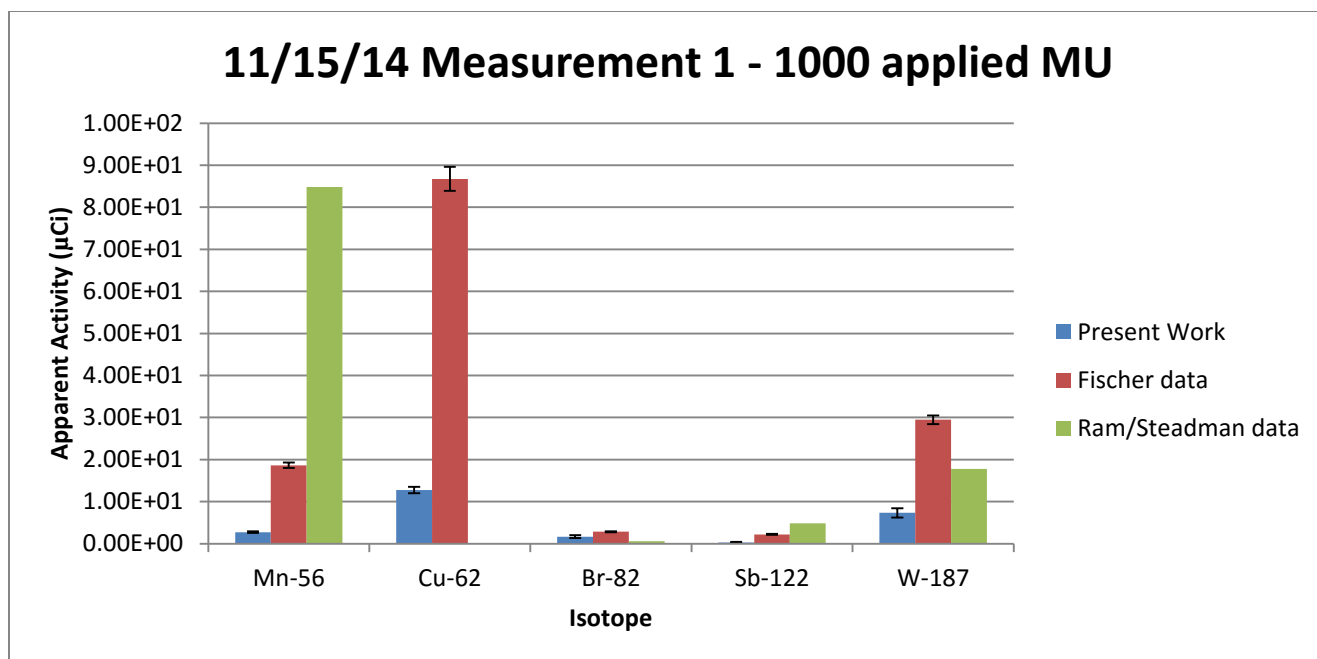


**Figure 3.9:** Apparent activity comparison between data sets after total application of 1000 MU with an MLC applied to the field.

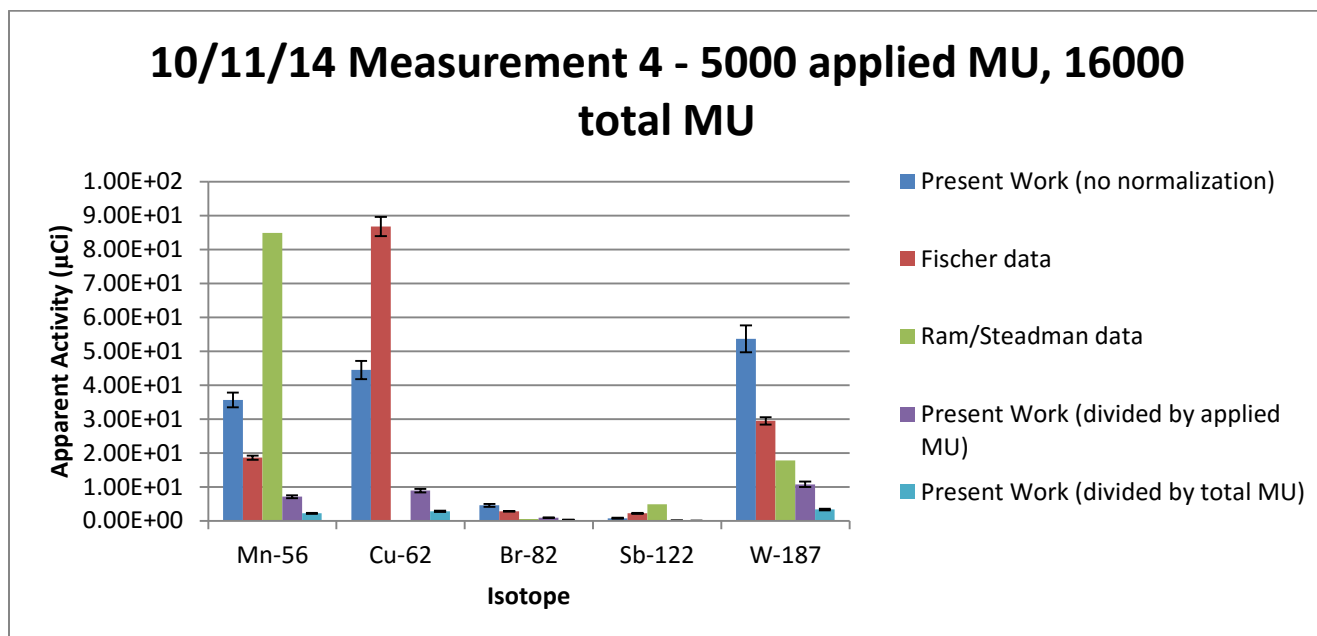


**Figure 3.10:** Apparent activity comparison between data sets after final application of 5000 MU, bringing the total applied MU count to 16000. Also shown is the comparison between the different normalization schemes. No applied MLC.



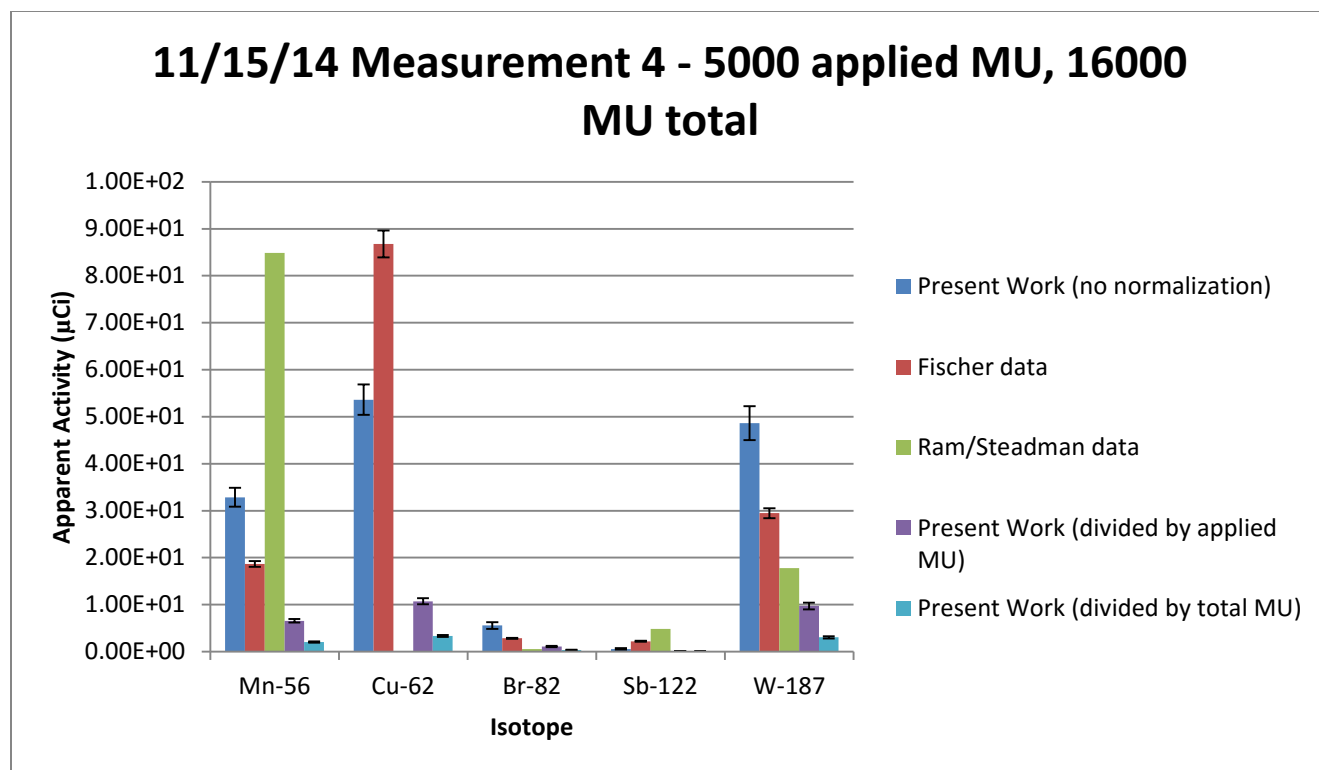


**Figure 3.11:** Apparent activity comparison between data sets after final application of 5000 MU, bringing the total applied MU count to 16000. Also shown is the comparison between the different normalization schemes. MLC was applied here.

		No Normalization (16000 MU)		Normalized to Total MU (16000 MU)	
Isotope		Apparent Activity ( $\mu\text{Ci}$ )	Activity error	Apparent Activity ( $\mu\text{Ci}$ )	Activity error
Mn-56	w/o MLC	3.56E+01	2.16E+00	2.23E+00	1.35E-01
	w/ MLC	3.28E+01	2.00E+00	2.05E+00	1.25E-01
Cu-62	w/o MLC	4.45E+01	2.70E+00	2.78E+00	1.69E-01
	w/ MLC	5.36E+01	3.25E+00	3.35E+00	2.03E-01
Br-82	w/o MLC	4.56E+00	4.42E-01	2.85E-01	2.76E-02
	w/ MLC	5.56E+00	7.24E-01	3.47E-01	4.53E-02
W-187	w/o MLC	5.37E+01	3.98E+00	3.35E+00	2.49E-01
	w/ MLC	4.86E+01	3.62E+00	3.04E+00	2.26E-01
Sb-122	w/o MLC	7.44E-01	1.40E-01	4.65E-02	8.72E-03
	w/ MLC	5.64E-01	1.71E-01	3.52E-02	1.07E-02

**Table 3.2:** Apparent Activity summary for analyzed isotopes. Data without normalization represents total activity after application of 16000 MU. Data normalized to total MU shows activity of isotope per 1000 MU after application of 16000 MU.

## Chapter 4

### Discussion

This project set out to determine the potential activation products produced after beam operation at energies above 10 MeV. After running a 15 MV beam for 16000 MU, the gamma spectra observed post-beam termination yielded several radioisotopes previously observed in other studies. Gamma energies above 400 keV were primarily considered and interestingly, no gamma peaks above 1348 keV were found. This was peculiar because previously published results listed several isotopes ( $^{24}\text{Na}$ ,  $^{28}\text{Al}$ ,  $^{57}\text{Ni}$ ) above this range (Ahlgren et al., 1988; Ram & Steadman, 2014; Thomadsen et al., 2014). Additionally, other higher energy gamma peaks found in other studies ( $^{56}\text{Mn}$ ,  $^{82}\text{Br}$ ) were not detected in this work.

A potential reason for these discrepancies is that the Falcon 5000 detector used in these measurements included a neutron probe which may have affected the detector response at low energies. It is also possible that certain detector settings may have affected the response at higher energies as well, since the highest energy peak (1348 keV) was only detected after altering the position of the detector such that it was directly under the beam aperture. Placement of the detector volume at the isocenter of the beam was utilized by several different researchers and may possibly lead to better signal detection. The measurements made at these positions are presented in Figures 3.3 and 3.4 and show the same isotopes found at the other detector positions along with small gamma peaks at 1046 and 1346 keV corresponding to  $^{124}\text{Sb}$  and  $^{64}\text{Cu}$ , respectively. Future experiments can be conducted with altered detector position and energy settings to determine whether gamma peaks above this energy exist for this particular linac.

It should be noted that, in spite of the myriad differences between researchers' methodologies in the type of linac analyzed, energy output, type of detector used, and detector position, there is remarkable agreement in many of the activated isotopes found. This would imply the presence of many common materials used in the manufacturing of these medical linacs, as well as similarly available accessories present in the treatment rooms. Although a complete analysis of the materials used in the construction of the linac studied was not possible in this work, the similarity to activated isotopes found in other studies implies that many materials are shared between the various types of Varian model linacs.

One of the defining features of this project was the source detector geometry. Whereas other investigators placed the detector at the beam isocenter, placement of the detector 30 cm from the solid water phantom in this study had the benefit of more accurately simulating radiation therapist positioning during patient set up. The addition of the solid water phantom also aided in simulating potential patient scatter into the detector face. However, due to the complex geometry involved, direct determination of detector efficiency was not possible and necessitated the use of 3D modeling via the ISOCS software package. Verification that the response of the ISOCS software matched a considerably simpler geometry (Figure 3.5 a – c) provided confidence that the software was capable of yielding accurate detector efficiencies for the geometry and range of energies used in this work. Even so, the ISOCS modeling did pose some challenges.

Based on previous studies, it has been shown that the treatment head and target are the primary source of induced activity. However, the materials used in the construction of this linac model and the actual size of these components are unknown. Simplifying this system involved the 3D modeling of a two-piece system only: target and solid water phantom. Modeling of the

solid water phantom was simple and straightforward, but due to the unknown characteristics of the target and treatment head, several simplifying assumptions were made. First, the target was modeled as a spherical point source in order to prevent self-attenuation at low energies. Second, only the target was modeled and tungsten was chosen as the material most likely to be used. These assumptions greatly simplified the linac system for efficiency calculation purposes due to the omissions of shielding, collimators, and other materials used in the linac treatment head construction. The resulting efficiency curve (Figure 3.7) seemed to be a good approximation when compared to the results from the simpler geometry from Figure 3.5c, but it may be possible to improve the calculated efficiency with a more detailed 3D modeling and knowledge of the construction materials used. Other considerations include taking measurements primarily with the detector volume at the beam isocenter in order to more readily verify detector efficiency.

The weighting factors used for efficiency calculations were arbitrarily chosen to approximate the proportional amount of radioactivity present between the components being modeled. This was especially difficult to determine given the fact that the materials used in the tungsten/water phantom system were so different from each other and their relative activity concentrations unknown. This scenario was also present in the check source geometry simulation, but was slightly simplified with the notion that the modeled polyurethane housing had a negligible activity concentration. Thus, the values that were used were arbitrarily chosen to best approximate the proportional amount of activity for the given item.

It should also be noted that this project was particularly unique because of the comprehensive efficiency modeling involved. The efficiency of the Falcon 5000 HPGe detector was verified at three different distances using three different sources representing a range of energies, and at each distance the efficiency matched very well with the simulated sources

produced by ISOCS. This has not been done before and it validated both the ISOCS software as an integral tool for modeling the efficiency of complex systems and the characterization of the Falcon 5000 HPGe detector with the software. Having such a comprehensive model of the efficiency also shows that the calculated apparent activities are accurate for the given geometry of our modeled experimental system.

Apparent activities were calculated for the five most prominent isotopes ( $^{56}\text{Mn}$ ,  $^{62}\text{Cu}$ ,  $^{82}\text{Br}$ ,  $^{122}\text{Sb}$ ,  $^{187}\text{W}$ ) detected in this work in order to be compared with the same isotopes presented in other studies. Two previous investigations conducted by Fischer et al. (2008) and Ram and Steadman (2014) were used as a template for the apparent activity analysis. These studies evaluated apparent activities due to activation products from Varian medical linacs different from the model used in the present work. Of particular interest are large discrepancies between the detected isotopes observed in the two studies. This is most likely caused by differences in key experimental parameters including linac model, beam energies, irradiation time, detector type, source-detector geometry and efficiency calibration. However, despite these differences, similar isotopes were observed and the five isotopes listed above were found in all studies including this work. Other isotopes observed in all studies included  $^{64}\text{Cu}$  and  $^{124}\text{Sb}$ , however these were only detected in this work when measurements were made with the detector volume at the beam isocenter (Figure 2.2). The bulk of the measurements reported in this work focused on the apparent activity build-up between beam operations, of five isotopes ( $^{56}\text{Mn}$ ,  $^{62}\text{Cu}$ ,  $^{82}\text{Br}$ ,  $^{122}\text{Sb}$ ,  $^{187}\text{W}$ ) detected using the source-detector shown in Figure 2.1. Although  $^{64}\text{Cu}$  and  $^{124}\text{Sb}$  were not detected during those measurements, it is reasonable to assume that they were present but could not be detected due to the source-detector geometry. The two isotopes were only observed following repositioning of the detector volume at the isocenter of the beam. This is in

good agreement with the results of both Fischer et al. (2008) and Ram and Steadman (2014) who observed all of the seven isotopes discussed above using an identical isocenter geometry.

The apparent activity analysis showed wide discrepancies between the calculated activities between each of the projects as shown in Figures 3.8 – 3.11. Even with different normalization schemes, there was little similarity between the three sets of data. The differences can most likely be attributed to the variations in experimental variables between the different investigations.

It is important to note that, in spite of these differences, each of the calculated apparent activities is very low, i.e., in the microcurie and lower range. The observation that the common isotopes detected are all in the microcurie range, despite changes in linac workload and detector positioning, implies that the total amount of additional activity present post-beam operation is likely limited to a few hundred microcuries. Although dose rate data was not collected during these measurements, they were measured by Fischer et al. (2008) and Ram and Steadman (2014). Given the similarity between the apparent activity ranges between those two prior investigations and this one, the annual dose to a radiation therapist working in the vicinity of the linac analyzed in this present work can be extrapolated to lie somewhere within the range of values estimated by Fischer et al. (2008) and Ram and Steadman (2014) for Varian machines, those values being 2.53 mSv and 3.15 mSv, respectively. This is within the range of acceptable annual occupational dose limits and should not be a problem for radiation therapists.

## Chapter 5

### Conclusion

The primary aim of the project involved quantifying the amount of activity from activated isotopes that arose after operating a Varian 21iX medical linac at 15 MV for 16000 MU. A Falcon 5000 HPGe detector, was used to measure gamma spectra of the activation products which were then compared with previously published results. Although it was not possible to determine the exact location of the activated materials, several studies have indicated that the linac treatment head and target are the primary sources of much of the induced radiation and, as such, both were considered in the 3D modeling of the experimental system in order to determine detector efficiency which was used to calculate apparent activities of the activation products.

The following activation products were identified from the Varian 21iX linac:  $^{56}\text{Mn}$  (848 keV),  $^{62}\text{Cu}$  (511 keV),  $^{82}\text{Br}$  (555, 1041 keV),  $^{99}\text{Mo}$  (778 keV),  $^{122}\text{Sb}$  (564 keV), and  $^{187}\text{W}$  (480, 617, 686 keV). These were identical to the activation products observed in other studies using different Varian linac models. Apparent activities were calculated for the five isotopes ( $^{56}\text{Mn}$ ,  $^{62}\text{Cu}$ ,  $^{82}\text{Br}$ ,  $^{122}\text{Sb}$ , and  $^{187}\text{W}$ ) similarly found in works by Fischer et al. (2008) and Ram and Steadman (2014). Estimated apparent activities for all activation products measured in this work were in the microcurie range which is in qualitative agreement with the findings of studies on other Varian linac models. No significant differences were observed between spectra acquired with or without MLCs. Slight changes in gamma spectra were noted following changes in source-detector geometry. For example,  $^{64}\text{Cu}$  and  $^{124}\text{Sb}$  were only observed when the sensitive volume of the detector was placed at the beam isocenter.



Future investigations can be conducted to obtain a deeper understanding of the activated isotopes present. Although the Falcon detector did not measure signals above 1348 keV, it is possible that settings can be adjusted for energy measurements above that range. Detector positioning can also be changed in order to simplify the geometry used for a more verifiable efficiency measurement. Placing the detector volume at the beam isocenter resulted in the detection of additional isotopes not observable at the primary source-detector geometry used in this work. Further investigation into the isotopes detected in the beam isocenter geometry immediately after beam termination may result in the detection of shorter lived and/or lower energy isotopes not detected in the primary geometry. It is also possible to utilize the MLC differently in order to determine how a more closed MLC field will affect the activated isotopes detected. Currently a 20 cm x 20 cm field was created with the MLC by opening the primary jaws to 25 cm x 25 cm. Creating a smaller field size and allowing a larger volume of MLC leaves to be subjected to beam radiation may yield different results.

In summary, the results of this work demonstrate that a Falcon detector can be used for rapid identification of activation products from high energy medical linacs such as the Varian 21iX. This data, in conjunction with Monte Carlo modeling, are capable of yielding estimates of apparent activity from each activation product thus allowing an estimate of doses to both personnel and patients in radiation therapy facilities.

## References

- Ahlgren, L., & Olsson, L.E. (1988). Induced activity in a high-energy linear accelerator. *Physics in Medicine and Biology*, 33(3), 351-354.
- Almen, A., Ahlgren, L., & Mattsson, S. (1991). Absorbed dose to technicians working at accelerators for radiation therapy. *Physics in Medicine and Biology*, 36(6), 815-822.
- Brusa, A., Cesana, A., Stucchi, C., Terrani, M., & Zanellati, F. (2008). Long term activation in a 15 MeV radiotherapy accelerator. *Medical Physics*, 35(7), 3049-3053.  
doi:10.1118/1.2936223
- Canberra Industries. (2009). *Falcon 5000: Characterization Report*. Meriden, CT: Canberra Industries
- Canberra Industries. (2011). *Falcon 5000: User Manual*. Meriden, CT: Canberra Industries
- Canberra Industries. (2012). *Model S573 ISOCS Calibration Software: Technical Reference Manual*. Meriden, CT: Canberra Industries
- Fischer, H.W., Tabot, B.E., & Poppe, B. (2006). Activation processes in a medical linear accelerator and spatial distribution of activation products. *Physics in Medicine and Biology*, 51, N461-N466. doi:10.1088/0031-9155/51/24/N02
- Fischer, H.W., Tabot, B., & Poppe, B. (2008). Comparison of activation products and induced dose rates in different high-energy medical linear accelerators. *Health Physics*, 94(3), 272-278.

- Followill, D.S., Stovall, M.S., Kry, S.F., & Ibbott, G.S. (2003). Neutron source strength measurements for Varian, Siemens, Elekta, and General Electric linear accelerators. *Journal of Applied Clinical Medical Physics*, 4(3), 189-194. doi:10.1120/1.571671
- Hendee, W.R., Ibbott, G.S., and Hendee, E.G. (2005). *Radiation Therapy Physics* (3<sup>rd</sup> ed.). Hoboken, NJ: John Wiley & Sons, Inc.
- Howard, S., & Starovoitova, V.N. (2015). Target optimization for the photonuclear production of radioisotopes. *Applied Radiation and Isotopes*, 96, 162-167.
- Howell, R.M., Kry, S.F., Burgett, E., Hertel, N.E., & Followill, D.S. (2009). Secondary neutron spectra from modern Varian, Siemens, and Elekta linacs with multileaf collimators. *Medical Physics*, 36(9), 4027-4038. doi:10.1118/1.3159300
- Khan, F.M., & Gibbons, J.P. (2014). *Khan's The Physics of Radiation Therapy* (5<sup>th</sup> ed.). Philadelphia, PA: Lippincott Williams & Wilkins
- Kim, K.Y., Kwak, J., Park, S.H., Choi, E.K., Kim, J.H., Lee, S., Song, S.Y., & Ahn, S.D., (2009). Identification of neutron-induced isotopes in Varian LINAC system. *IFMBE Proceedings*, 25(3), 616-619.
- Knoll, G.F. (1999). *Radiation Detection and Measurement* (3<sup>rd</sup> ed.). Hoboken, NJ: John Wiley & Sons, Inc.
- Konefal, A., Dybek, M., Zipper, W., Lobodziec, W., & Szczucka, K. (2005). Thermal and epithermal neutrons in the vicinity of the Primus Siemens biomedical accelerator. *Nukleonika*, 50(2), 73-81.
- Konefal, A., Polaczek-Grelik, K., & Zipper, W. (2008). Undesirable nuclear reactions and induced radioactivity as a result of the use of the high-energy therapeutic beams

generated by medical linacs. *Radiation Protection Dosimetry*, 128(2), 133-145.  
doi:10.1093/rpd/ncm318

Konefal, A., Orlef, A., Laciak, M., Ciba, A., & Szewczuk, M. (2012). Thermal and resonance neutrons generated by various electron and x-ray therapeutic beams from medical linacs installed in polish oncological centers. *Reports of Practical Oncology and Radiotherapy*, 17, 339-346.

Naseri, A., & Mesbahi, A. (2010). A review on photoneutrons characteristics in radiation therapy with high-energy photon beams. *Reports of Practical Oncology and Radiotherapy*, 15, 138-144. doi:10.1016/j.rpor.2010.08.003

Nath, R., Boyer, A.L., La Riviere, P.D., McCall, R.C., & Price, K.W. (1986). Neutron measurements around high energy x-ray radiotherapy machines. *American Association of Physicists in Medicine Task Group 27*.

Ram, R., & Steadman, I. (2014). *Determination of activation products and resulting dose rates for the Varian Truebeam*. Retrieved from <http://crpa-acrp.org/home/wp-content/uploads/2014/11/Ram-Steadman-Determination-of-Activation-Products-and-Resulting-Dose-Rates-for-the-Varian-TrueBeam-R03.pdf>

Roig, M., Panettieri, V., Ginjaume, M., & Sanchez-Reyes, A. (2004). Photonuclear isotope characterization of a Siemens KDS 18MV linac head. *Physics in Medicine and Biology*, 49, N243-N246. doi:10.1088/0031-9155/49/14/N05

Saeed, M.K., Poppe, B., & Fischer, H.W. (2015). Direct air activation measurements at a 15-MV medical linear accelerator. *Radiation Protection Dosimetry*, 163(2), 233-237.  
doi:10.1093/rpd/ncu149

Starovoitova, V.N., Tchelidze, L., Wells, D.P. (2014). Production of medical radioisotopes with linear accelerators. *Applied Radiation and Isotopes*, 85, 39-44.

- Thomadsen, B., Nath, R., Bateman, F.B., Farr, J., Glisson, C., Islam, M.K., LaFrance, T., Moore, M.E., Xu, X.G., & Yudelev, M. (2014). Potential hazard due to induced radioactivity secondary to radiotherapy: the report of task group 136 of the American Association of Physicists in Medicine. *Health Physics*, 107(5), 442-460.
- Wambersie, A., & Gahbauer, R.A. (1996). Medical applications of electron linear accelerators. CERN Accelerator School (CAS): Cyclotrons, linacs and their applications. Cern 96-02, 4 March 1996. CERN, Geneva, pp 229 – 248.
- Yamaguchi, I., Terada, H., Takahashi, M.N., & Sugiyama, H. (2008) Quantitative activation analysis of the target assemblies of a medical linear accelerator. *Journal of Radioanalytical and Nuclear Chemistry*, 278(2), 505-507. doi:10.1007/s10967-008-0913-2

## Curriculum Vitae

### Timothy Thatcher

#### *Medical Physics Master Student*

2699 Rimpacific Cir.

Las Vegas, NV 89146

[thatct1@unlv.nevada.edu](mailto:thatct1@unlv.nevada.edu)

(831) 430-8915 (Cell)

## Education

- 8/2013 – 11/2015     **University of Nevada, Las Vegas**, Las Vegas, NV 89154  
*M.S. in Medical Physics*  
Thesis title: “Measurement of Neutron Activation from High Energy  
Varian Linear Accelerators”  
Advisor: Steen Madsen, Ph.D
- 9/2005 – 6/2009     **University of California, Irvine**, Irvine, CA 92697  
*B.S. in Physics with a Biological Emphasis*

## Research/Academic Experience

- 1/2015 – Present     **Comprehensive Cancer Centers of Nevada**, Las Vegas, NV 89169  
*Clinical Student*  
Assisted with and learned about the clinical duties of a medical physicist.
- 1/2014 – Present     **University of Nevada**, Las Vegas, NV 89154  
*Graduate Researcher*  
Measurement of Neutron Activation from High Energy Varian Linear  
Accelerators.
- 7/2015     **American Association of Physicists in Medicine (AAPM) Conference  
2015**, Anaheim, CA 92802  
*Presenter*  
Presented poster for research project “Measurement of Neutron Activation  
from High Energy Varian Linear Accelerators”
- 8/2014 – 5/2015     **University of Nevada**, Las Vegas, NV 89154  
*Graduate Assistant in School of Allied Health Sciences*  
Independent Instructor for Undergraduate Core Course: Inquiry and Issues  
in Health Sciences.
- 1/2014 – 5/2014     **University of Nevada**, Las Vegas, NV 89154  
*Graduate Assistant in School of Allied Health Sciences*  
Independent Instructor for Undergraduate Core Course: Radiation Science.

- 8/2013 – Present      **University of Nevada**, Las Vegas, NV 89154  
*Graduate and Professional Student Association (GPSA)*  
 Health Physics Representative to UNLV Student Government for Graduate and Professional Students.
- 3/2015                    **University of Nevada**, Las Vegas, NV 89154  
*Technology Coordinator - GPSA Research Forum*  
 Served as Technology Coordinator for the Graduate and Professional Student Research Forum.
- 8/2013 – 5/2014      **University of Nevada**, Las Vegas, NV 89154  
*Bookstore Advisory Committee*  
 Served as GPSA liaison to UNLV Bookstore Advisory Committee.
- 6/2007 – 6/2009      **University of California**, Irvine, CA 92697  
*Research Assistant in Physics Department*  
 Collected and interpreted data on phase transitions of a bubble raft to low amplitude oscillatory shear.
- 9/2007 – 3/2009      **University of California**, Irvine, CA 92697  
*Math & Physics Tutor*  
 Worked one on one with students teaching Calculus and Physics at the California Alliance for Minority Participation office.
- 10/2008                **Society for Advancement of Chicanos/Hispanics and Native Americans in Science (SACNAS) Conference**, Salt Lake City, UT 84101  
*Presenter*  
 Presented poster for research project “Response of Foam to Low Amplitude Oscillatory Shear”

### **Professional Memberships**

- 2015 – Present      **Phi Kappa Phi Honors Society** – Member
- 2015 – Present      **American Association of Physicists in Medicine (AAPM)** - Member
- 2013 – 2016        **Graduate and Professional Student Association** – Health Physics Representative